DOI: 10.1002/((please add manuscript number))
Article type: Review

A New Twist for Materials Science: The Formation of Chiral Structures using The Angular Momentum of Light

Takashige Omatsu[1,2,], Katsuhiko Miyamoto[1,2], Kohei Toyoda[1,2], Ryuji Morita[3], Yoshihiko Arita[2,4] and Kishan Dholakia[1,4,5]*

Takashige Omatsu 1,2,*, Katsuhiko Miyamoto 1,2, Kohei Toyoda 1,2
1. Graduate School of Engineering, Chiba University, Japan
2. Molecular Chirality Research Center, Chiba University, Japan
E-mail: omatsu@faculty.chiba-u.jp

Ryuji Morita 3
3. Graduate School of Engineering, Hokkaido University, Japan

Yoshihiko Arita 2,4
2. Molecular Chirality Research Center, Chiba University, Japan
4. SUPA, School of Physics and Astronomy, University of St Andrews, United Kingdom

Kishan Dholakia 1,4,5
1. Graduate School of Engineering, Chiba University, Japan
4. SUPA, School of Physics and Astronomy, University of St Andrews, United Kingdom
5. Department of Physics, College of Science, Yonsei University, Seoul 03722, South Korea

Keywords: (singular optics, optical vortices, orbital angular momentum, spin angular momentum, laser materials processing, chiral structured materials)

Abstract

Recent work has shown that irradiation with light possessing orbital angular momentum and an associated phase singularity, that is an optical vortex, *twists* a variety of materials. These include silicon, azo-polymer, and even liquid-phase resins to form various helically structured materials. Here, we review the unique helical-structured materials created and the novel fundamental phenomena enabled by this interaction between both the spin and orbital angular momentum of light with matter. Such light-induced helical-structured materials will potentially lead to advanced photonic devices, for instance, metamaterials for ultra-sensitive detection and reactions for chiral chemical composites.

1. Introduction

In 1992, Allen *et.al.* theoretically proposed that light carries orbital angular momentum (OAM), as a consequence of its associated helical wavefront and on-axis phase singularity. Such fields have an azimuthal phase term denoted $\exp(i\ell\phi)$, where ℓ is an integer (either positive or negative) and ϕ is the azimuthal angle [1–3]. The OAM of light has led to a myriad of new physical effects and various applications particularly at the microscopic scale. This includes optical trapping and manipulation [4–6], optical telecommunications [7,8], quantum physics [9], and 'super resolution' microscopy with a spatial resolution beyond the diffraction limit [10–12]. New applications for OAM fields have also been proposed in environmental optics and free-space telecommunication. As an example OAM states can potentially propagate though air turbulence with lower degradation than a conventional Gaussian beam [13,14]. New physical effects include studies such as the rotational Doppler effect originating from interactions of such fields and rotating objects that may provide new technologies for remote sensing of rotating bodies in astrophysics [15,16].

In this area of original physical demonstrations, recent studies have shown that irradiation by such an OAM field can *twist* materials, such as metal, silicon, azo-polymer, and even a liquid-phase resin with the help of spin angular momentum (SAM) of circularly polarized light with the rotating electric field. This can thus shape helical nano/micro-structures [17–24].

Going beyond fundamental aspects, *twisted* materials created by such OAM fields may provide a new understanding of interactions between optical fields and matter on the subwavelength scale that may reveal new physics, *e.g.* spin-orbit coupling effects or unconventional opto-mechanical effects for moving beyond traditional forms of optical manipulation. Furthermore, *twisted* materials created by such OAM fields, will provide a new understanding of interactions between optical fields and matter on a subwavelength scale. For example, the *twisted* materials manifest the role of both SAM and OAM of light fields and the coupling of SAM and OAM

(so-called spin-orbit coupling) effects. This coupling is key not only for understanding fundamental physics but also for controlling optical material structures.

Conventional optical tweezers rely on the field gradients near the diffraction limited focus of a laser beam to hold mesoscopic particles solely with focused light beams. However, the technique often fails to efficiently trap and manipulate particles at the nanoscale because the gradient force scales with the volume of the particle and is proportional to the particle's polarisability. In this domain, advanced materials science and nanofabrication technologies have made remarkable progress in structured devices, *e.g.*, photonic crystals, metamaterials and metasurfaces. These devices offer novel trapping geometries to enhance the interaction between optical fields and materials at the nanoscale. Furthermore, these devices allow the control of optical wavefronts including those of an optical vortex possessing OAM. Such optical devices have also shown unconventional opto-mechanical effects [25,26] and offer a novel class of optical manipulation allowing new degrees of freedom in light-matter interactions.

Materials processing with a light field possessing OAM can have significant potential in other emergent fields. For instance, arrays of *twisted* nanostructures may find applications in lab-on-a-chip systems [27] for detection of chiral chemical composites and for control of chiral chemical reactions [28]. Applications may include fabrication of optical waveguides for space- and mode-division multiplexing systems using optical vortex modes. Understanding the interplay between an OAM field and appropriate materials is thus a key for the successful fabrication of nanostructured materials.

In this article, we review the unique structured materials and novel fundamental phenomena involved when a light field with both SAM and OAM interacts with appropriate materials. We describe the physical interaction as well as mechanical consequences on the samples in question. These state-of-the-art fundamental studies and the resulting structures will lead to next-generation applications exploiting the unique features of light fields possessing angular momentum.

2. OAM and total angular momentum

In this section, we review a variety of methods of generating OAM fields, and address the interactions between OAM light fields and matter of selected materials. Generated OAM fields enable us to study fundamental physics such as spin-orbit coupling effects as well as offering unconventional opto-mechanical effects in micromanipulation.

2.1 OAM field generation[29]

The most common method to generate a propagating OAM field with a vortex at beam center is to transform an incident planar wavefront into a spiral wavefront by employing a mode convertor. A good example is a spiral phase plate (SPP) possessing an azimuthally increasing phase retardation (or segmented steps). This imparts the appropriate azimuthal phase shift onto the wavefront [30,31]. Alternatively a SAM-OAM convertor, termed a "*q*-plate", can create a spiral wavefront from circularly polarized light with a plane wavefront [32,33]. The OAM of the light field is delineated by an integer index ℓ denoting the number of complete 2π cycles of azimuthal phase around the mode circumference as mentioned earlier. The complete mode description also requires a further integer index p that denotes the number of radial nodes (p+1 rings), which ideally would be zero (a single ringed OAM field) [29]. The methods described above may lead to undesired higher-order radial p components, resulting in reduced mode purity. An alternative route is to use a computer-controlled spatial light modulator (SLM) (or a digital micro-mirror device) that freely modulates the azimuthal phase and amplitude of the incident light field [34], thereby synthesizing very high quality OAM modes without any undesired higher-order radial components at a desired wavelength.

In the last few decades, subwavelength-scale, structured devices, such as photonic crystals, metamaterials [35] and metasurfaces, have been developed to manipulate electromagnetic waves, with the specific aim to achieve novel physical properties that do not exist in natural materials. In particular, these structured devices enable the design of appropriate optical wavefronts at the

nano/micro scale. The advantage can particularly be to offer mode conversion schemes whose footprint is very small and compatible with on chip geometries. We describe two recent examples of metasurfaces that lead to OAM fields with the associated inclined wavefronts and phase singularity (optical vortex) at beam center.

Various plasmonic metasurfaces formed of V-shaped antennas have been demonstrated to provide an arbitrary geometrical phase shift by tuning the shape and orientation of each antenna depending on the polarization of the incident light fields. This can yield helical wavefronts, though they typically suffer from a low energy conversion efficiency (~25%) owing to the intrinsic loss of a single-layer metasurface [36,37].

Ma et.al. proposed a novel planar chiral metasurface which converts circularly polarized light into an OAM field, and focuses the converted field onto a given plane [38]. This metasurface was formed of a hexagonally-placed elliptical silver antenna, so as to modulate the local geometrical phase of the incident light. With this device, circularly polarized light was converted into an optical vortex carrying OAM. It is noteworthy that the thickness of this metasurface was less than λ/4; thus, this device has a potential to be integrated into compact optical vortex generation systems with a high energy conversion efficiency of >40%.

Several small-scale non-metasurface approaches have also been reported in various materials such as liquid crystals [39], polymers [40] and glass [41].

2.2 Spin-orbital angular momentum coupling

A field with an optical vortex may carry an OAM of $\ell\hbar$ per photon, arising from its helical wavefront due to an azimuthal phase term, $\exp(i\ell\phi)$. This is to be contrasted with circularly polarized light possessing a SAM, $s\hbar$ per photon ($s = \pm 1$), associated with a rotating electric field around the propagation axis. Thus, a circularly polarized optical vortex possesses a total angular momentum (TAM), $J\hbar$, where $J = \ell + s$, defined as the sum of the OAM and SAM owing to both inclined wavefront and polarization contributions [42,43]. This TAM was experimentally

confirmed by observing both the orbital and spinning motion of trapped micro-particles using optical micromanipulation techniques [44–49]. Rotating particles in light fields with spin and orbital angular motion can exhibit different effects in optical traps. This is a manifestation of the fact that spin angular momentum is intrinsic and creates a torque on particles to cause them to rotate around their own axis. Orbital angular momentum can in fact be both intrinsic or extrinsic, where in the latter case the particle may be observed to orbit around the beam axis [43]. It is worth noting that even optical vortices with $J = 0$, exhibit non-zero finitely-apertured TAM, $\tilde{J}(\ell, s)$, defined as $2\pi \int_0^r j_{\ell,s}(r)\, r dr$[18], thereby yielding orbital motion of the trapped particles[43]. Here, $j_{\ell,s}(r)$ is the total angular momentum density of the optical vortex field with ℓ and s, and r is the radial axis, respectively [18].

We note that tightly focused circularly polarized light enables the generation of a longitudinal electric field with a helical phase in a homogenous and isotropic medium (SAM-OAM coupling) [47,50]. Also, the scattering of circularly polarized light by a small particle generates an optical vortex in the output field. Furthermore, such SAM-OAM coupling of light occurs during beam propagation in anisotropic crystals [51], or optical fibers [52,53]. For instance, Petersen *et.al.* demonstrated the mirror symmetry breaking of the scattering of light with a gold nanoparticle on the surface of a nanofiber [54]. Additionally, the evanescent nearfield generated from nanofibers or the interface between two different materials typically possesses SAM-induced OAM, *i.e.* the generation of nearfield OAM light.

A transverse shift of an incident circularly polarized light beam via reflection or refraction at a planar interface is a further method of SAM-OAM coupling: the so-called "spin-Hall effect of light"[50,55,56]. Such SAM-OAM coupling effects can easily break the degeneracy of two optical vortices with the same TAM, and offer new light- matter interactions.

3. Helical structures

In this section, we review unique structured materials, such as helical structures of metal, silicon, polymer, and monocrystalline needles, created by the interplay between a light field possessing angular momentum and an appropriate material sample.

3.1 Helical metal needles

Helical nanoneedles remain challenging to fabricate by employing a conventional laser processing or even advanced chemical processes. Such nanostructures can be exploited potentially to create chiral plasmonic metasurfaces for selective identification of the chirality and optical activity of molecules and chemical composites. An OAM field can be employed for materials processing, and it may *twist* the materials to form helical structures [17]. In this section we show examples of state-of-the-art fabrication of such nanostructures.

A pulsed OAM field with a vortex at beam center (wavelength: 1.06 μm, pulse width: 30 ns, pulse energy: 0.3 mJ) was generated by a SPP. It carried an azimuthal index (topological charge) ℓ of unity. The optical vortex pulse was focused by a lens to form an annular spot with a diameter of ~65 μm onto a metal surface of tantalum. As shown in **Figure 1**, a needle-like structure was formed at the center of the ablated zone, *i.e.* the dark core of the optical vortex, with a smooth outline, and was *twisted* azimuthally in the clockwise direction. The tip curvature and height of the *twisted* needle were measured to be <100 nm and ~10 μm respectively. When the sign of the OAM of the incident field was reversed, the needle was seen to twist in the counter-clockwise direction [18]. These observations indicate that the handedness of the OAM field determines the twisting direction (chirality) of the needle, thereby providing clear evidence that the OAM of the optical vortex plays a central role in the formation of the nanoneedle structure at the dark core for this material. The tip curvature of the needle was found to be approximately inversely proportional to numerical aperture (NA) of the focusing lens and its minimum value was measured to be <40 nm, corresponding to <1/25 of the optical vortex wavelength where the optical vortex pulse fluence was fixed to ~9 J/cm^2.

To understand how the overall wavefront helicity taking into account OAM, SAM and TAM, influences the outcome, the generated needle structures were further investigated with light fields possessing various values of ℓ, s, and J.

The handedness, *i.e.* sense of twisting direction, of the needles was determined only by the sign of ℓ, regardless of the sign of s. However, the spiral density of the needles (this value is defined as the winding number divided by the length of the needle) increased with $|J|$, and it was determined by J rather than ℓ and s [18]. It should be noted that two optical vortices with the same TAM are degenerate and may lead to the same form of helical needle. Namely, the needle created by a linearly polarized second-order (J=2, ℓ=2, s=0) OAM field exhibited the same chirality and spiral density as those of that created by circularly polarized first-order (J=2, ℓ=1, s=1) OAM field. This degeneracy between two OAM fields with the same TAM is theoretically supported by the space-integrated azimuthal optical radiation forces over the whole beam aperture produced by these two fields [18].

Notably, such helical structures formed by OAM field illumination have also been demonstrated in a bulk copper (Cu) [57] and silver (Ag) and gold (Au) thin films, which are well-known to support surface plasmons. In particular, helical Ag needles formed on a thin film, which are dubbed “chiral plasmonic nanojets”, were successfully demonstrated by Syubaev et.al. [20]. A visible wavelength OAM beam (wavelength: 532 nm, pulse energy: 40-230 nJ, pulse duration: 4 ns, $\ell = \pm 1$) was focused to form an annular spot with a diameter of 2-4 μm onto a sample Ag film (thickness: ~500 nm), deposited by e-beam evaporation onto a silica glass substrate. *Twisted* nanojets were formed by a single laser pulse where the *twisted* direction was determined by the handedness of the optical vortex (**Figure 2**). The formation of such *twisted* nanojets involves several steps, namely (i) the accumulation of revolving melted material at the dark vortex core of the irradiating OAM field via thermo-capillary forces, (ii) the formation of a liquid nanojet undergoing a Plateau-Rayleigh hydrodynamic instability, (iii) the ejection of

spinning melted droplets and, (iv) the formation of a *twisted* nanojet. The resulting nanojets typically exhibited very fine tips with a curvature radius of 10-20 nm.

Syubaev *et.al.* also demonstrated, interestingly, the formation of *twisted* plasmonic nanoneedles with a tip curvature of ~10 nm on Ag and Au films by the irradiation of a nanosecond visible (wavelength: 532 nm) pulse with a vortex-shaped beam without any OAM, which is dubbed "spiral-shaped light", generated by a binary spiral axicon [20]. Such *twisted* nanoneedles are formed not owing to OAM, but are a consequence of thermo-capillary mass transport arising from the temperature gradient created by the spatially non-uniform laser irradiation (**Figure 3**) [58]. They also mentioned that the initial surface temperature distribution of the irradiated metal plays a key role to induce the chiral mass transport of the melted metal. These should provide us with a new insight for such materials. Also note that the spiral density (up to 9 μm^{-1}) of the fabricated nanoneedles is associated with the spiral-arm number of the irradiated light.

3.2 Silicon and dielectric structures

Monocrystalline silicon (Si) is a standard material for general electronics and has been widely studied for the development of photonic devices, including photonic crystals, photonic integrated circuits, and photovoltaic cells. The creation of helical Si structures may allow us to provide another degree of freedom to add to the aforementioned Si photonic devices. Several researchers have demonstrated the formation of Si structured materials by the irradiation of OAM fields with pulse durations ranging from nanosecond to femtosecond time scales.

A circularly polarized nanosecond OAM pulse (pulse energy: 0.1 mJ, J=2, annular spot diameter: ~24 μm) was irradiated onto a plane of (100) monocrystalline silicon substrate [22]. A chiral cone of silicon with a nanometer-scale (~100 nm) tip curvature and a micrometer-scale (~1 μm) height was formed, and its chirality was controlled by the handedness of the incident OAM pulse.

The use of ultrafast (picosecond - femtosecond) lasers for irradiation may minimize optothermal effects and collateral damage of the material surfaces. For instance, Rahimian et.al. created cone-shaped nanostructures with a *twist* and extremely smooth circular rim (without any debris arising from laser-induced thermal effects) on a silicon substrate by the deposition of a single femtosecond OAM pulse with zero-TAM, *i.e.* $\ell = \pm 1$ and $s = \mp 1$ (**Figure 4**) [59]. The fabricated nanostructures exhibited a tip curvature of ~70 nm, and a height of 350-1000 nm. However, it is typically difficult to form *twisted* structured materials by the irradiation of optical fields even with OAM, because of significant vaporization of the materials.

Kohmura *et.al.* demonstrated the fabrication of *non-twisted* nanoneedles with a width of 310 nm and a height of ~600 nm on Cr/Au multi-layers upon a silicon substrate by the irradiation of vacuum ultraviolet (~160 nm) femtosecond OAM pulses generated from a free electron laser (**Figure 5**) [60]. Notably when a relatively high energy (~0.6 mJ) picosecond (~20 ps) OAM pulse was irradiated on a silicon substrate, an over 10 μm high needle was fabricated without any helical feature. Several overlaid OAM pulses also enabled the needle to be grown on the silicon substrate, resulting in a needle with a height of ~40 μm (**Figure 6**) [22].

An OAM field with an annular intensity profile collects the melted silicon within its dark vortex core through the vaporization-induced recoil pressure and thermal diffusion effects. To reveal how the optical vortex pulse illumination creates the silicon needle, the solid-liquid hydrodynamics of the silicon needle formation was recently observed with an ultra-high speed camera [22]. The silicon needle was recrystallized on a sub-microsecond time scale after the irradiation of an optical vortex pulse. Fluid-dynamics simulations also clarified that the radial inward mass transport of the melted silicon, arising from thermal-diffusion effects, acts as a collective force on the melted silicon to form these cone-shaped nanostructures. The theoretical models supported all the previous experiments concerning the silicon-needle formation **(Figure 7)**. In general, an ultrafast laser pulse induces the recrystallized silicon to form polycrystalline structures [61–65]. Such micro-second scale motion of the melted silicon in the

optical vortex pulse illumination results in the high crystallinity of the silicon needle, which is identified by the electron diffraction analyses [21]. The OAM should provide a spin on the melted silicon, resulting in the efficient accumulation of the melted silicon in the dark core forming the needle on the substrate.

The laser surface machining of metals, semiconductors and insulators is itself attracting a growing interest for industry applications based on the hydrophobic or hydrophilic property of the processed solid surfaces [66,67]. Femtosecond lasers also enable the spontaneous creation of periodic sub-wavelength surface ripples along the normal direction to the beam polarization, the so-called "laser-induced periodic surface structures" (LIPSS) [68,69]. The LIPSS formation should be dominated by the polarization of light and the excitation of surface plasmon polaritons. However, a beam-shaping technique, providing structured wavefront in a single laser beam, may offer the possibility to create further complex LIPSS [70].

Nivas et.al. demonstrated femtosecond laser-based surface structuring by employing an OAM field with a vortex that also had various polarization states [70]. In this study, femtosecond pulses from a Ti:Sapphire laser (pulse duration: ~35 fs) were converted to (i) a radially polarized beam, (ii) an azimuthally polarized beam, and (iii) an OAM field with ℓ=±1 by employing a *q*-plate and a quarter-wave plate. One hundred overlaid pulses (pulse energy: ~48 μJ) with different polarization states resulted in annular craters with different LIPSSs on the silicon surface. A central null region of the crater, corresponding to the optical vortex present in the field, was composed of a large number of nanoparticles. An inner ring-shaped region (high-fluence region) in the ablated annular crater exhibited unique micron-scale textures, including spiral grooves, preferentially directed along the polarization. In contrast, subwavelength ripples were oriented along the normal direction to the polarization at the outer edge of the optical vortex (low fluence region) (**Figure 8**). Such unique surface structures can be explained by the Sipe-Drude approach, taking into account the carrier-dependent variation effects of the dielectric permittivity of the target material irradiated with femtosecond pulses [70].

Furthermore, Taylor et. al. discovered that focused circularly polarized femtosecond laser pulses (wavelength: 800nm, number of overlaid pulses: 100~3000, pulse energy: ~350nJ, pulse width: 150 fs) created permanent chiral structures with a core diameter of <50nm, and a core depth of ~500nm inside fused silica glass [71]. Such chiral structures are formed by memory effects of nonlinear ionization and erasure induced by irradiation of multiple femtosecond laser pulses (**Figure 9**) [71].

3.3 Helical surface reliefs

So far we have seen the formation of chiral nanoneedles on metal and silicon surfaces, in which the process does not involve chemical reactions leading to material transformation. We now progress to discuss the case where chemical reactions can play a role. Azo polymers are of interest as azobenezene has polarisation sensitivity and thus may offer advantages over standard photoresist in terms of its insensitivity to stray light, broadband optical response and relative resistance to over exposure (so multiple irradiations can be used). Upon non-uniform illumination of azo-polymers, light absorption leads to non-uniform cis-trans photoisomerization, which causes spatially anisotropic photo-fluidity [72–74]. Subsequently, mass transport occurs by the optical scattering force from a bright region towards a dark region along the polarization direction of the illuminated light forming an intensity-sensitive surface relief on an azo-polymer film (**Figure 10**).

Several theoretical models concerning light-induced mass-transport of azo-polymers [75] have been proposed; for instance, an interaction model between dipoles and the gradient of an optical electric field [76]; a light-induced pressure model [77]; a diffusion model based on a random walk motion [78]; a photoisomerization force model due to the polymer's elasticity and the optical gradient force *etc* [75]. However, there are only a few theoretical studies on how an azo-polymer film is deformed by irradiation of an optical field with OAM.

Ambrosio et.al. discovered the formation of a helical surface relief (termed "spiral relief" in their work), in which tightly focused higher-order OAM fields caused azimuthal mass-transport owing to the interference between the longitudinal and transverse optical fields creating a spiral surface relief with a shallow depth (10-20 nm) (**Figure 11**) [79]. Furthermore, the formation of a helical surface relief having a micron-scale depth was demonstrated by using a lower-order OAM field ($|\ell|\leq 2$) with the aid of SAM (**Figure 12**) [23]. Such wavefront-sensitive surface relief formation is briefly reviewed in this section.

An azo-polymer film with an absorption band in the blue-green wavelength region undergoes photoisomerization upon green laser light irradiation. A continuous-wave green laser output (wavelength: 532 nm) was converted to a circularly polarized first-order optical vortex by utilizing a spatial light modulator together with a quarter-wave plate. The generated optical vortex was focused by a high-NA objective lens, yielding a micron-sized annular spot with an optical density of 1-2 kW/cm^2 on the azo-polymer film.

Interestingly, the degeneracy between two fields with the same TAM was broken in the surface relief formation on the azo-polymer film. In fact, only a circularly polarized optical vortex with positive (negative) OAM and positive (negative) SAM forced the orbital motion of the azo-polymers towards the clockwise (counter-clockwise) direction to establish a wavefront-sensitive helical structure. Conversely, even the circularly polarized optical vortex with non-zero TAM inhibited the helical structure formation when the beam carried opposite signs of OAM and SAM, *i.e.* positive OAM and negative SAM and vice versa.

Such degeneracy breaking can be explained by an imhomogeneous spatial distribution of the angular-momentum density of the irradiating field. However, there have been only a few theoretical studies on the deformation of isotropic and homogeneous materials, such as an azo-polymer film, under radiation pressure. Thus, there is a good scope to understand how homogeneous materials are deformed by the OAM and SAM.

Barada et.al. proposed an analytical formula for the time-averaged OAM-field-induced optical radiation force in an isotropic and homogeneous material under the paraxial approximation [80]. The resulting optical radiation force, **F**, can be expressed as follows:

$$F(r,\phi,z) \propto \chi_r \left(\frac{\sqrt{1-s^2}}{2}\frac{\partial A_\ell^2}{\partial r}\left(-\cos(\phi)\cdot \boldsymbol{e_x} + \sin(\phi)\cdot \boldsymbol{e_y}\right) + \left(\frac{1}{2}\frac{\partial A_\ell^2}{\partial r} - \ell s\frac{A_\ell^2}{r}\right)\cdot \boldsymbol{e_r}\right) +$$

$$\chi_i \left(\ell\frac{\sqrt{1-s^2}}{2}\frac{A_\ell^2}{r}\left(\sin(\phi)\cdot \boldsymbol{e_x} + \cos(\phi)\cdot \boldsymbol{e_y}\right) + \left(\ell\frac{A_\ell^2}{r} - \frac{s}{2}\frac{\partial A_\ell^2}{\partial r}\right)\cdot \boldsymbol{e_\phi} + 2kA_\ell^2\cdot \boldsymbol{e_z}\right), \quad (1)$$

where $\mathbf{e}_r$, $\mathbf{e}_\phi$, and $\mathbf{e}_z$ are the unit vectors along the r, ϕ, and z-axes, respectively; $\mathbf{e}_x$ and $\mathbf{e}_y$ are also unit vectors for the polarization state in a Cartesian coordinate system; ℓ and s are the azimuthal charge of OAM and the magnitude of SAM; $A_\ell(r)$ is the radial amplitude of OAM field with ℓ; k is the wavenumber; and χ ($=\chi_r+i\chi_i=2+2i$) is the macroscopic complex electric susceptibility, respectively.

The radial amplitude $A_\ell(r)$ is given as

$$A_\ell(r) = \frac{A_0}{\sqrt{\ell!}}\left(\sqrt{2}\frac{r}{\omega_0}\right)^{|\ell|}\exp\left(-\frac{r^2}{\omega_0^2}\right), \quad (2)$$

where ω_0 is the radius of the optical field.

When the field possesses the positive product of OAM and SAM, *i.e.* both positive (negative) OAM and SAM, the radial force plays the role of a restoring force to confine the materials into the dark vortex core, and the azimuthal force drives the orbital motion of the materials either clockwise or counter-clockwise around the dark core. When the product of the OAM and SAM is negative, on the other hand, the optical vortex generates a repulsive radial force, which impacts the efficient confinement of the materials inside the dark vortex core. Also, the azimuthal force reverses inside and outside of the dark core, so that the smooth orbital motion

of the materials is prevented (**Figure 13**). These results indicate that only fields with a positive product of OAM and SAM enables the formation of helical structures, thereby breaking the degeneracy among such fields with the same TAM.

A helical surface relief can be formed by the illumination of a focused circularly polarized Gaussian beam without any associated OAM. However, unlike in the case of illumination by an OAM field, the fabricated helical surface relief was further transformed into a non-helical structure in the final form upon further exposure (**Figure 14**) [81]. These experiments suggest that SAM-OAM coupling may occur in an isotropic and homogeneous medium such as an azo-polymer film, inducing orbital motion and forming a helical surface relief as an intermediate form, even without any OAM. However, as soon as this helical structure is formed, breaking the spatial symmetry of the azo-polymer film, the SAM-OAM coupling is prevented, which destroys the helical surface relief itself. Nakata et.al. recently demonstrated the parallel fabrication of helical surface reliefs on an azo-polymer film by employing an interference pattern formed of six circularly polarized optical fields with SAM (**Figure 15**) [82]. Chiral structures induced by circularly polarized optical fields are also observed in a uniform liquid-crystal film via light-induced elastic distortions [83].

Helical surface reliefs structured on a thin gold film enable the generation of nearfield OAM light on a sub-wavelength scale by the SAM-OAM coupling effects between a circularly polarized plane-wave light field and the helical surface relief structure. The generated nearfield OAM light leads to a further nanoscale mass-transport of azo-polymers [84]. These studies will pave the way towards the development of novel photonic devices with chirality, particularly, in combination with nanoscale vortex generation based on the structured materials, *e.g.*, metamaterials.

3.4 Self-written helical fiber

Continuous-wave ultraviolet (UV) light or near-infrared ultrashort pulses can activate cross-linked polymerization within appropriate resins (photopolymerization), so as to create three-

dimensional transparent micro-objects with a high spatial resolution. Since its realization, photopolymerization has gained widespread applications, including micro-optics [85], mechanical microstructures [86] and polymer crystallography [87]. In fact, three-dimensional (3D) chiral microstructures have been demonstrated through two-photon polymerization by irradiation of OAM light fields produced by an SLM [88], or coaxial interference of a femtosecond vortex beam with a plane wave (**Figure 16**) [89].

Interestingly, self-focusing and self-trapping of the incident beam occur upon initiating polymerization due to a permanent refractive index change of the resin [90,91]. As a consequence of nonlinear self-focusing of the optical field, photopolymerization forms a waveguide fiber (the so-called "laser-induced self-written fiber") (**Figure 17**) [92]. This unique nonlinear optical phenomenon has been widely studied with different types of beams including Bessel (**Figure 18**) [93] and Laguerre-Gaussian beams (**Figure 19**) [94]. However, self-written fiber studies have yet to fully exploit more complex incident beam wavefronts beyond the standard planar wavefront form.

Recently, Lee *et. al.* investigated a self-written fiber with an optical vortex carrying OAM [24]. The UV cure resin is typically made of photoinitiators, monomers and oligomers. Irradiation of a continuous-wave UV laser (wavelength: 405 nm) excites the photoinitiators to be radicals, which are highly reactive to the monomers and oligomers, thereby inducing photopolymerization within a time lag of ~0.1 second depending on the optical power. The polymerized material exhibits a higher refractive index in comparison with that of the uncured resin, resulting in self-focusing and self-trapping effects of the incident light beams to establish self-written fibers.

The incident optical vortex beams with an optical power of 1-3 mW and ℓ of ±1 were focused to an annular spot (radius: 1-2 μm) onto the resin surface where twisting or helical fibers were formed along the beam propagation direction (**Figure 20**). Importantly, the chirality or

handedness of the helical fibers was determined by the sign of the azimuthal charge of the incident beams, *i.e.* the handedness of the optical vortex.

Higher order beams with ℓ of 2, 4 created multiple or branched microfibers with the corresponding number of OAM modes. For the case of $\ell = \pm 2$ (or 4), the polymerized fiber was split into two (or four) branches that attracted each other to form a double (quad) helix coiled around each other with the clockwise (or counter-clockwise) direction (**Figure 21**). The polymerized fibers thus manifested the chirality and azimuthal charge of the OAM of the irradiating optical vortex.

Such a fiber branching occurs in the process of the nonlinear self-focusing owing to a transverse modulation instability in the incident light field [95]. Thus, in a higher order OAM field, the optical vortex breaks up into single-charged optical vortices, *i.e.* spatial solitons or microfibers, with helical trajectories, and together form a bundle of helical microfibers.

A theoretical model for the propagation of a UV light field in a cure resin, as presented by Kewitsch and Yariv [91], is given as follows:

$$\frac{\partial E}{\partial z} = \frac{1}{2k_b}\nabla_T^2 E + ik_0\Delta n'(r,t)E - \frac{\alpha}{2}E, \quad (3)$$

$$k_b = n_b k_0, \quad (4)$$

$$k_0 = \omega/c, \quad (5)$$

where n_b is the background refractive index, α is the absorption coefficient, ω is the angular frequency of the optical field, c is the speed of light in a vacuum, $k_0 = \omega/c$, and ∇^2_T is the transverse Laplacian describing the beam diffraction. Here, the paraxial wave equation for the slowly-varying scalar electric field envelope $E(r, t)$, propagating along the z-axis, is assumed. Also, the refractive index response, $\Delta n'(r, t)$, due to photopolymerization is given by

$$\Delta n'(r,t) = \Delta n_0' \left(1 - \exp\left(-\frac{1}{U_0}\int_0^{t-\tau}|E|^2 dt\right)\right), \quad (6)$$

where τ is the time-lag required for effective photopolymerization from the laser irradiation, $\Delta n_0'$ (=0.04) is the refractive index change before and after polymerization, and U_0 (=500 J/cm^2) is the critical exposure fluence needed for photopolymerization [91]. Numerical simulations, based on the nonlinear paraxial wave equation and the time-integrated photopolymerization effect, support all the experimental observations for optical vortices with various azimuthal charges (**Figure 22**). Indeed, the simulated results clearly indicate self-focusing and self-trapping with the formation of a fiber along the *z*-axis throughout the beam propagation where the induced fiber was *twisted* at around *z* = 100 μm forming a helical structure.

We note that the filamentation of spatial solitons in the third-order (saturable) nonlinearities was observed in a nano-colloidal suspension with negative polarizability due to the modulation instability [96]. The incident vortex beam with higher order OAM, carrying ~1 W of optical power, was split into a necklace beam with several bright spots, *i.e.* spatial solitons (**Figure 23**). Further, the number of observed bright spots corresponded to the topological charge of the incident optical vortex beam.

Such self-written helical fibers, manifesting helical trajectories of the optical vortex solitons [97] will open up a range of new possibilities for the use of structured light to photopolymerization and more broadly to such applications in optical vortex waveguides for optical communications and particle manipulations. Helical microfibers may also offer a new testbed for the studies of mode-generation/conversion and optical manipulation.

4. Conclusions

Light fields possessing OAM are associated with a helical wavefront and typically possess a dark vortex core. Their unusual properties can pave the way towards many new research

applications in laser materials processing: in particular, the OAM field *twists* materials to form a wide range of helical micro/nano-structures, *e.g.*, helical microneedles, helical surface reliefs, helical and branched fibers. The chirality (or handedness) of the structured materials can be controlled by the handedness of the field, *i.e.* the sign of the OAM with the aid of the SAM associated with the rotating electric field of the circular polarization, in which SAM accelerates (or decelerates or inhibits) the formation of helical structured materials. The SAM-OAM coupling effects can also have interesting consequences even with the same TAM, and the coupling term significantly contributes to the formation of helical structured materials and potentially manifests new fundamental physical phenomena.

We remark that several other non-optical techniques to fabricate chiral structures have been proposed; for instance, direct laser writing photopolymerization, DNA-based self-assembly, deposition of gaseous precursors initiated by focused electron or ion beam etc [98]. These have successfully enabled the development of metamaterials showing circular dichroism in the visible region. The creation of chiral structures by illumination of OAM beam is promising to fabricate chiral structures at room temperature and in atmosphere and will provide new research opportunities. However, the optical technique lacks maturity when compared to the above non-optical techniques with great design freedom on a large-scale area.

Non-naturally existing structured materials such as photonic crystals should enable the creation of OAM fields towards the nanoscale, thereby yielding further advanced helical nanostructures. Such helical nano/micro-structures formed by optical vortex illumination will potentially open the door to develop a wide range of advanced nanomaterial sciences and technologies. These could include metasurfaces for selective identification of chiral chemical composites and the enhancement of chiral chemical reactions, waveguides for space- and mode-division multiplexing in telecommunications, and industrial applications based on the hydrophobic or hydrophilic properties of materials.

Acknowledgments

The authors acknowledge support from the Japan Society for the Promotion of Science (JSPS) KAKENHI Grants (JP 16H06507; JP 17K19070; JP 18H03884). We thank the UK Engineering and Physical Sciences Research Council for support through Grant EP/P030017/1.

References

[1] L. Allen, M. W. Beijersbergen, R. J. C. Spreeuw, J. P. Woerdman, *Phys. Rev. A* **1992**, *45*, 8185.

[2] M. Padgett, J. Courtial, L. Allen, *Phys. Today* **2004**, *57*, 35.

[3] M. J. Padgett, F. M. Miatto, M. P. J. Lavery, A. Zeilinger, R. W. Boyd, *New J. Phys.* **2015**, *17*, 023011.

[4] T. Kuga, Y. Torii, N. Shiokawa, T. Hirano, Y. Shimizu, H. Sasada, *Phys. Rev. Lett.* **1997**, *78*, 4713.

[5] M. Padgett, R. Bowman, *Nat. Photonics* **2011**, *5*, 343.

[6] K. Dholakia, T. Čižmár, *Nat. Photonics* **2011**, *5*, 335.

[7] J. Wang, J. Y. Yang, I. M. Fazal, N. Ahmed, Y. Yan, H. Huang, Y. Ren, Y. Yue, S. Dolinar, M. Tur, A. E. Willner, *Nat. Photonics* **2012**, *6*, 488.

[8] N. Bozinovic, Y. Yue, Y. Ren, M. Tur, P. Kristensen, H. Huang, A. E. Willner, S. Ramachandran, *Science (80-.).* **2013**, *340*, 1545.

[9] G. Molina-Terriza, J. P. Torres, L. Torner, *Nat. Phys.* **2007**, *3*, 305.

[10] I. Heller, G. Sitters, O. D. Broekmans, G. Farge, C. Menges, W. Wende, S. W. Hell, E. J. G. Peterman, G. J. L. Wuite, *Nat. Methods* **2013**, *10*, 910.

[11] T. Watanabe, Y. Iketaki, T. Omatsu, K. Yamamoto, M. Sakai, M. Fujii, *Opt. Express* **2003**, *11*, 3271.

[12] M. Kamper, H. Ta, N. A. Jensen, S. W. Hell, S. Jakobs, *Nat. Commun.* **2018**, *9*, 4762.

[13] Y. Li, L. Yu, Y. Zhang, *Opt. Express* **2017**, *25*, 12203.

[14] D. Liu, Y. Wang, H. Yin, *Appl. Opt.* **2015**, *54*, 10510.

[15] M. P. J. Lavery, F. C. Speirits, S. M. Barnett, M. J. Padgett, *Science (80-.).* **2013**, *341*, 537.

[16] Z. Liu, Y. Liu, Y. Ke, J. Zhou, Y. Liu, H. Luo, S. Wen, *Opt. Express* **2017**, *25*, 11564.

[17] K. Toyoda, K. Miyamoto, N. Aoki, R. Morita, T. Omatsu, *Nano Lett.* **2012**, *12*, 3645.

[18] K. Toyoda, F. Takahashi, S. Takizawa, Y. Tokizane, K. Miyamoto, R. Morita, T. Omatsu, *Phys. Rev. Lett.* **2013**, *110*, 143603.

[19] S. Syubaev, A. Zhizhchenko, A. Kuchmizhak, A. Porfirev, E. Pustovalov, O. Vitrik, Y. Kulchin, S. Khonina, S. Kudryashov, *Opt. Express* **2017**, *25*, 10214.

[20] S. Syubaev, A. Porfirev, A. Zhizhchenko, O. Vitrik, S. Kudryashov, S. Fomchenkov, S. Khonina, A. Kuchmizhak, *Opt. Lett.* **2017**, *42*, 5022.

[21] F. Takahashi, S. Takizawa, H. Hidai, K. Miyamoto, R. Morita, T. Omatsu, *Phys. Status Solidi Appl. Mater. Sci.* **2016**, *213*, 1063.

[22] F. Takahashi, K. Miyamoto, H. Hidai, K. Yamane, R. Morita, T. Omatsu, *Sci. Rep.* **2016**, *6*, 21738.

[23] M. Watabe, G. Juman, K. Miyamoto, T. Omatsu, *Sci. Rep.* **2014**, *4*, 4281.

[24] J. Lee, Y. Arita, S. Toyoshima, K. Miyamoto, P. Panagiotopoulos, E. M. Wright, K. Dholakia, T. Omatsu, *ACS Photonics* **2018**, *5*, 4156.

[25] W. Tsai, J. Huang, C. Huang, *Nano Lett.* **2014**, *14*, 547.

[26] G. Spektor, D. Kilbane, A. K. Mahro, B. Frank, S. Ristok, L. Gal, P. Kahl, D. Podbiel, S. Mathias, H. Giessen, F. J. Meyer Zu Heringdorf, M. Orenstein, M. Aeschlimann, *Science (80-.).* **2017**, *355*, 1187.

[27] Y. A. Vlasov, X.-Z. Bo, J. C. Sturm, D. J. Norris, *Nature* **2001**, *414*, 289.

[28] S. L. Cheng, C. Y. Chen, S. W. Lee, *Thin Solid Films* **2010**, *518*, S190.

[29] A. M. Yao, M. J. Padgett, *Adv. Opt. Photonics* **2011**, *3*, 161.

[30] M. W. Beijersbergen, R. P. C. Coerwinkel, M. Kristensen, J. P. Woerdman, *Opt. Commun.* **1994**, *112*, 321.

[31] G. A. Turnbull, D. A. Robertson, G. M. Smith, L. Allen, M. J. Padgett, *Opt. Commun.* **1996**, *127*, 183.

[32] L. Marrucci, C. Manzo, D. Paparo, *Phys. Rev. Lett.* **2006**, *96*, 163905.

[33] E. Karimi, B. Piccirillo, E. Nagali, L. Marrucci, E. Santamato, *Appl. Phys. Lett.* **2009**, *94*, 231124.

[34] N. Matsumoto, T. Ando, T. Inoue, Y. Ohtake, N. Fukuchi, T. Hara, *J. Opt. Soc. Am. A* **2008**, *25*, 1642.

[35] S. Zhang, Y.-S. Park, J. Li, X. Lu, W. Zhang, X. Zhang, *Phys. Rev. Lett.* **2009**, *102*, 023901.

[36] N. Yu, P. Genevet, M. A. Kats, F. Aieta, J. P. Tetienne, F. Capasso, Z. Gaburro, *Science (80-.).* **2011**, *334*, 333.

[37] P. Genevet, N. Yu, F. Aieta, J. Lin, M. A. Kats, R. Blanchard, M. O. Scully, Z. Gaburro, F. Capasso, *Appl. Phys. Lett.* **2012**, *100*, 013101.

[38] X. Ma, M. Pu, X. Li, C. Huang, Y. Wang, W. Pan, B. Zhao, J. Cui, C. Wang, Z. Zhao, X. Luo, *Sci. Rep.* **2015**, *5*, 10365.

[39] E. Brasselet, N. Murazawa, H. Misawa, S. Juodkazis, *Phys. Rev. Lett.* **2009**, *103*, 103903.

[40] E. Brasselet, M. Malinauskas, A. Žukauskas, S. Juodkazis, *Appl. Phys. Lett.* **2010**, *97*, 2.

[41] G. Ruffato, M. Massari, F. Romanato, *Opt. Lett.* **2014**, *39*, 5094.

[42] S. M. Barnett, *J. Opt. B Quantum Semiclassical Opt.* **2001**, *4*, S7.

[43] A. T. O'Neil, I. MacVicar, L. Allen, M. J. Padgett, *Phys. Rev. Lett.* **2002**, *88*, 053601.

[44] V. Garcés-Chávez, D. McGloin, M. J. Padgett, W. Dultz, H. Schmitzer, K. Dholakia, *Phys. Rev. Lett.* **2003**, *91*, 093602.

[45] H. He, M. E. J. Friese, N. R. Heckenberg, H. Rubinsztein-Dunlop, *Phys. Rev. Lett.* **1995**, *75*, 826.

[46] M. E. J. Friese, T. A. Nieminen, N. R. Heckenberg, H. Rubinsztein-Dunlop, *Nature* **1998**, *394*, 348.

[47] Y. Zhao, J. S. Edgar, G. D. M. Jeffries, D. McGloin, D. T. Chiu, *Phys. Rev. Lett.* **2007**, *99*, 15.

[48] Y. Arita, M. Mazilu, K. Dholakia, *Nat. Commun.* **2013**, *4*, 2374.

[49] Y. Arita, M. Chen, E. M. Wright, K. Dholakia, *J. Opt. Soc. Am. B* **2017**, *34*, C14.

[50] K. Y. Bliokh, F. J. Rodríguez-Fortuño, F. Nori, A. V. Zayats, *Nat. Photonics* **2015**, *9*, 796.

[51] T. A. Fadeyeva, V. G. Shvedov, Y. V. Izdebskaya, A. V. Volyar, E. Brasselet, D. N. Neshev, A. S. Desyatnikov, W. Krolikowski, Y. S. Kivshar, *Opt. Express* **2010**, *18*, 10848.

[52] N. Bozinovic, S. Golowich, P. Kristensen, S. Ramachandran, *Opt. Lett.* **2012**, *37*, 2451.

[53] A. E. Willner, H. Huang, Y. Yan, Y. Ren, N. Ahmed, G. Xie, C. Bao, L. Li, Y. Cao, Z. Zhao, J. Wang, M. P. J. Lavery, M. Tur, S. Ramachandran, A. F. Molisch, N. Ashrafi, S. Ashrafi, *Adv. Opt. Photonics* **2015**, *7*, 66.

[54] J. Petersen, J. Volz, A. Rauschenbeutel, *Science (80-.).* **2014**, *346*, 67.

[55] K. Y. Bliokh, Y. P. Bliokh, *Phys. Rev. Lett.* **2006**, *96*, 073903.

[56] K. Y. Bliokh, *Phys. Rev. Lett.* **2006**, *97*, 043901.

[57] T. Omatsu, K. Miyamoto, R. Morita, *Optical Vortices Illumination Enables the Creation of Chiral Nanostructures*, InTech, **2017**.

[58] S. Syubaev, A. Zhizhchenko, O. Vitrikc, A. Porfirev, S. Fomchenkov, S. Khonina, S. Kudryashov, A. Kuchmizhak, *Appl. Surf. Sci.* **2019**, *470*, 526.

[59] M. G. Rahimian, F. Bouchard, H. Al-Khazraji, E. Karimi, P. B. Corkum, V. R. Bhardwaj, *APL Photonics* **2017**, *2*, 086104.

[60] Y. Kohmura, V. Zhakhovsky, D. Takei, Y. Suzuki, A. Takeuchi, I. Inoue, Y. Inubushi, N. Inogamov, T. Ishikawa, M. Yabashi, *Appl. Phys. Lett.* **2018**, *112*, 123103.

[61] J. Bonse, S. Baudach, J. Krüger, W. Kautek, M. Lenzner, *Appl. Phys. A* **2002**, *74*, 19.

[62] J. Bonse, K.-W. Brzezinka, A. J. Meixner, *Appl. Surf. Sci.* **2004**, *221*, 215.

[63] U. Zywietz, A. B. Evlyukhin, C. Reinhardt, B. N. Chichkov, *Nat. Commun.* **2014**, *5*, 3402.

[64] S. V. Makarov, M. I. Petrov, U. Zywietz, V. Milichko, D. Zuev, N. Lopanitsyna, A. Kuksin, I. Mukhin, G. Zograf, E. Ubyivovk, D. A. Smirnova, S. Starikov, B. N. Chichkov, Y. S. Kivshar, *Nano Lett.* **2017**, *17*, 3047.

[65] S. Makarov, L. Kolotova, S. Starikov, U. Zywietz, B. Chichkov, *Nanoscale* **2018**, *10*, 11403.

[66] C. Guo, L. Feng, J. Zhai, G. Wang, Y. Song, L. Jiang, D. Zhu, *ChemPhysChem* **2004**, *5*, 750.

[67] X. Feng, L. Feng, M. Jin, J. Zhai, L. Jiang, D. Zhu, *J. Am. Chem. Soc.* **2004**, *126*, 62.

[68] C. Hnatovsky, V. Shvedov, W. Krolikowski, A. Rode, *Phys. Rev. Lett.* **2011**, *106*, 123901.

[69] O. J. Allegre, W. Perrie, S. P. Edwardson, G. Dearden, K. G. Watkins, *J. Opt.* **2012**, *14*, 085601.

[70] J. J. J. Nivas, S. He, A. Rubano, A. Vecchione, D. Paparo, L. Marrucci, R. Bruzzese, S. Amoruso, *Sci. Rep.* **2015**, *5*, 17929.

[71] R. S. Taylor, E. Simova, C. Hnatovsky, *Opt. Lett.* **2008**, *33*, 1312.

[72] A. Natansohn, P. Rochon, *Chem. Rev.* **2002**, *102*, 4139.

[73] H. Ishitobi, M. Tanabe, Z. Sekkat, S. Kawata, *Opt. Express* **2007**, *15*, 652.

[74] N. K. Viswanathan, D. Y. Kim, S. Bian, J. Williams, W. Liu, L. Li, L. Samuelson, J. Kumar, S. K. Tripathy, *J. Mater. Chem.* **1999**, *9*, 1941.

[75] Z. Sekkat, *Appl. Opt.* **2016**, *55*, 259.

[76] J. Kumar, L. Li, X. L. Jiang, D.-Y. Kim, T. S. Lee, S. Tripathy, *Appl. Phys. Lett.* **1998**, *72*, 2096.

[77] C. J. Barrett, P. L. Rochon, A. L. Natansohn, *J. Chem. Phys.* **1998**, *109*, 1505.

[78] P. Lefin, C. Fiorini, J. M. Nunzi, *Pure Appl. Opt.* **1998**, *9*, 323.

[79] A. Ambrosio, L. Marrucci, F. Borbone, A. Roviello, P. Maddalena, *Nat. Commun.* **2012**, *3*, 989.

[80] D. Barada, G. Juman, I. Yoshida, K. Miyamoto, S. Kawata, S. Ohno, T. Omatsu, *Appl. Phys. Lett.* **2016**, *108*, 051108.

[81] K. Masuda, S. Nakano, D. Barada, M. Kumakura, K. Miyamoto, T. Omatsu, *Opt. Express* **2017**, *25*, 12499.

[82] Y. Nakata, M. Yoshida, N. Miyanaga, *Sci. Rep.* **2018**, *8*, 13448.

[83] E. Brasselet, *Opt. Lett.* **2009**, *34*, 3229.

[84] K. Masuda, R. Shinozaki, Y. Kinezuka, J. Lee, S. Hashiyada, H. Okamoto, D. Sakai, K. Harada, K. Miyamoto, T. Omatsu, *Opt. Express* **2018**, *26*, 22197.

[85] S. Lightman, G. Hurvitz, R. Gvishi, A. Arie, *Optica* **2017**, *4*, 605.

[86] K. S. Paulsen, D. Di Carlo, A. J. Chung, *Nat. Commun.* **2015**, *6*, 6976.

[87] H.-J. Lee, Y.-R. Jo, S. Kumar, S. J. Yoo, J.-G. Kim, Y.-J. Kim, B.-J. Kim, J.-S. Lee, *Nat. Commun.* **2016**, *7*, 12803.

[88] S.-J. Zhang, Y. Li, Z.-P. Liu, J.-L. Ren, Y.-F. Xiao, H. Yang, Q. Gong, *Appl. Phys. Lett.* **2014**, *105*, 061101.

[89] J. Ni, C. Wang, C. Zhang, Y. Hu, L. Yang, Z. Lao, B. Xu, J. Li, D. Wu, J. Chu, *Light Sci. Appl.* **2017**, *6*, e17011.

[90] S. J. Frisken, *Opt. Lett.* **1993**, *18*, 1035.

[91] A. S. Kewitsch, A. Yariv, *Opt. Lett.* **1996**, *21*, 24.

[92] M. Kagami, T. Yamashita, H. Ito, *Appl. Phys. Lett.* **2001**, *79*, 1079.

[93] J. Ježek, T. Cižmár, V. Nedela, P. Zemánek, *Opt. Express* **2006**, *14*, 8506.

[94] R. Malallah, J. P. Ryle, J. T. Sheridan, J. J. Healy, I. Muniraj, D. Cassidy, *Appl. Opt.* **2018**, *57*, E80.

[95] M. F. Shih, C. C. Jeng, F. W. Sheu, C. Y. Lin, *Phys. Rev. Lett.* **2002**, *88*, 133902.

[96] J. Sun, S. Z. Silahli, W. Walasik, Q. Li, E. Johnson, N. M. Litchinitser, *Opt. Express* **2017**, *26*, 5118.

[97] A. Zannotti, F. Diebel, M. Boguslawski, C. Denz, *Adv. Opt. Mater.* **2017**, *5*, 1600629.

[98] J. Kaschke, M. Wegener, *Nanophotonics* **2016**, *5*, 510.

((Insert Figure here. Note: Please do not combine figure and caption in a textbox or frame.))

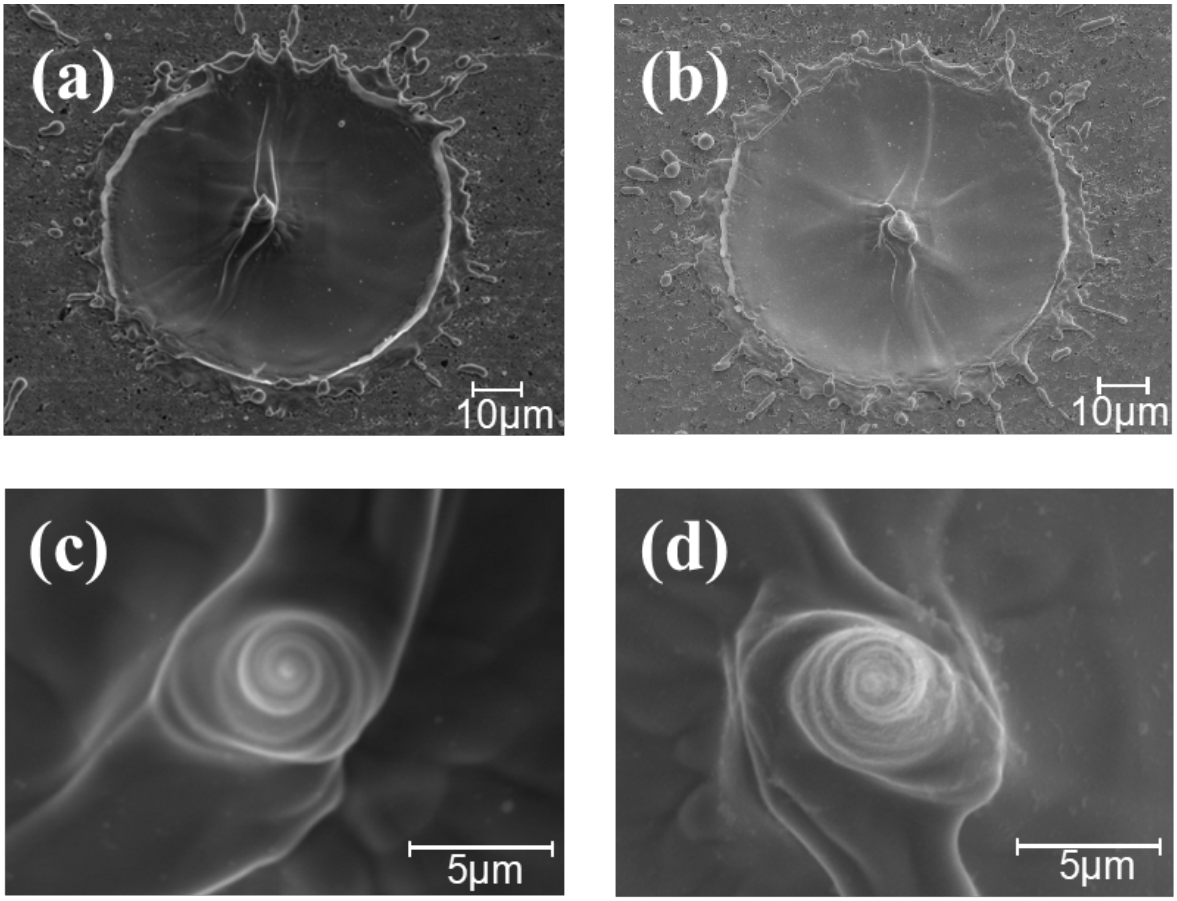

Figure 1.
Twisted tantalum nanoneedles fabricated by (a) left-handed OAM (J=-2) and (b) right-handed OAM (J=2), with magnified views in (c) and (d).

Reproduced with permission.[17] Copyright 2012, American Chemical Society.

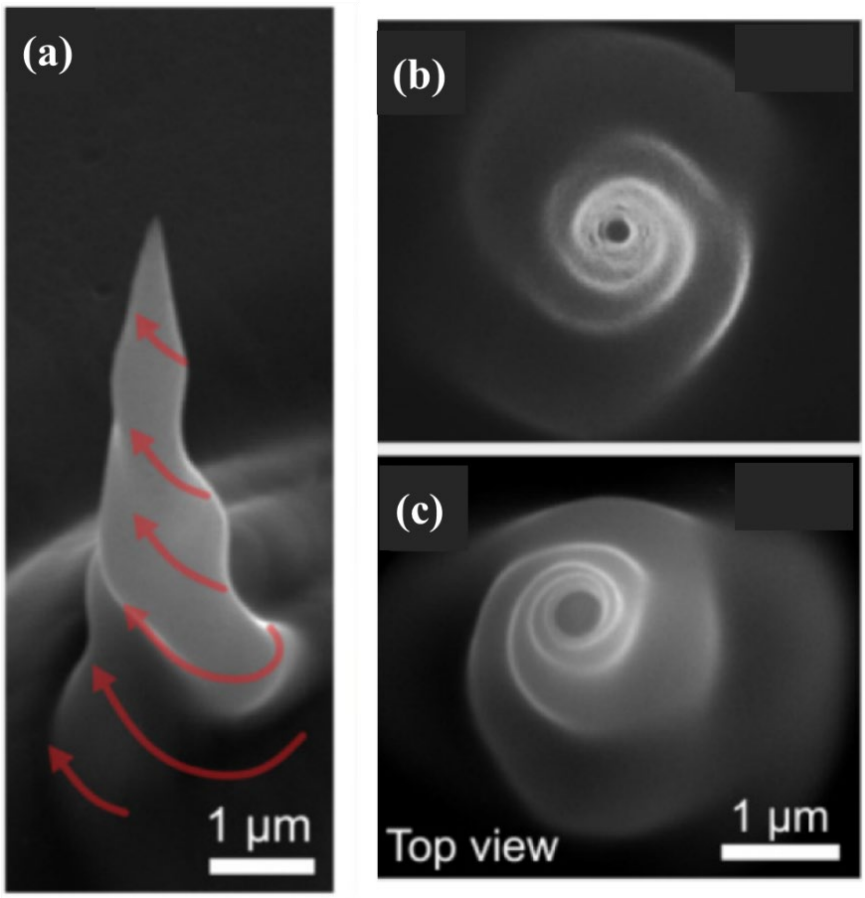

Figure 2.
Twisted silver nanojets. (a) Side-view with red arrows indicating the rotation direction. Top views of (b) left-handed and (c) right-handed Ag nanojets.

Reproduced with permission.[19] Copyright 2017, The Optical Society.

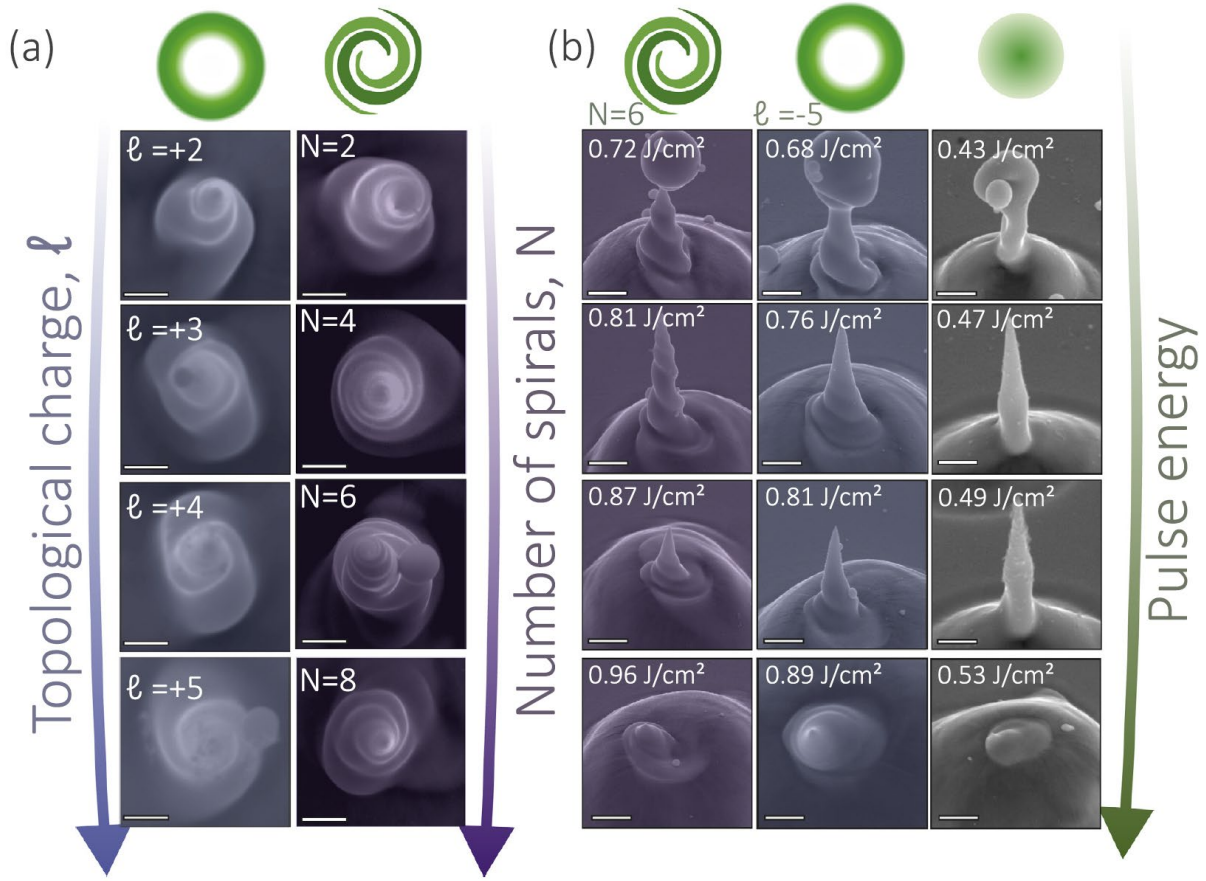

Figure 3.
Chiral silver nanoneedles fabricated on an Ag film with (a) various ℓ and spiral arm number N, (b) different pulse energy at N=6, ℓ=-5 and Gaussian beam.

Reproduced with permission.[58] Copyright 2019, Elsevier.

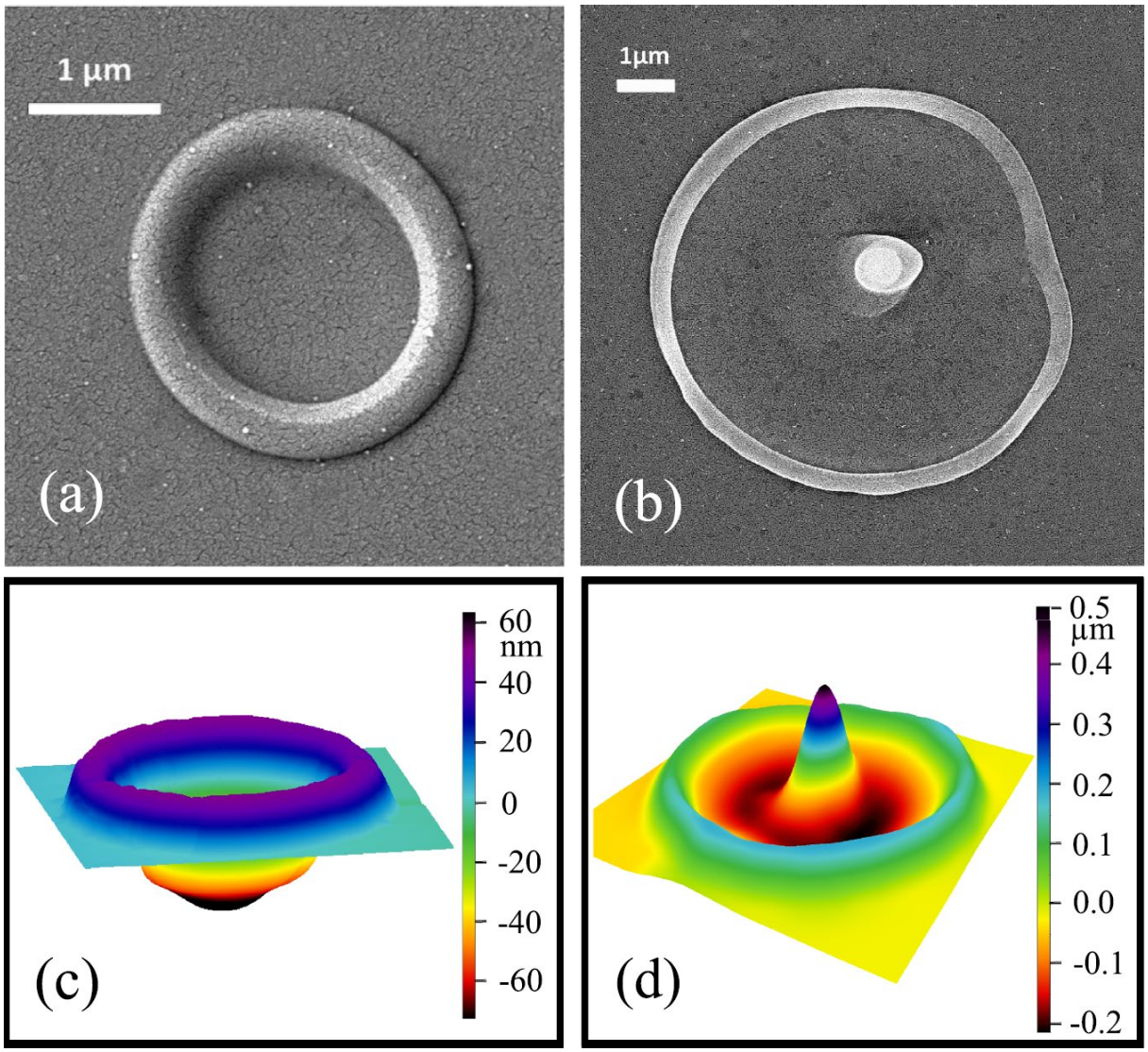

Figure 4.
SEM [(a) and (b)] and AFM [(c) and (d)] images of nanostructures created on p-type silicon by irradiation with a femtosecond vortex laser pulse (ℓ = -1, s = +1) with pulse energies of (a,c) 150 nJ and (b,d) 310 nJ.

Reproduced with permission. [59] Copyright 2017, American Institute of Physics.

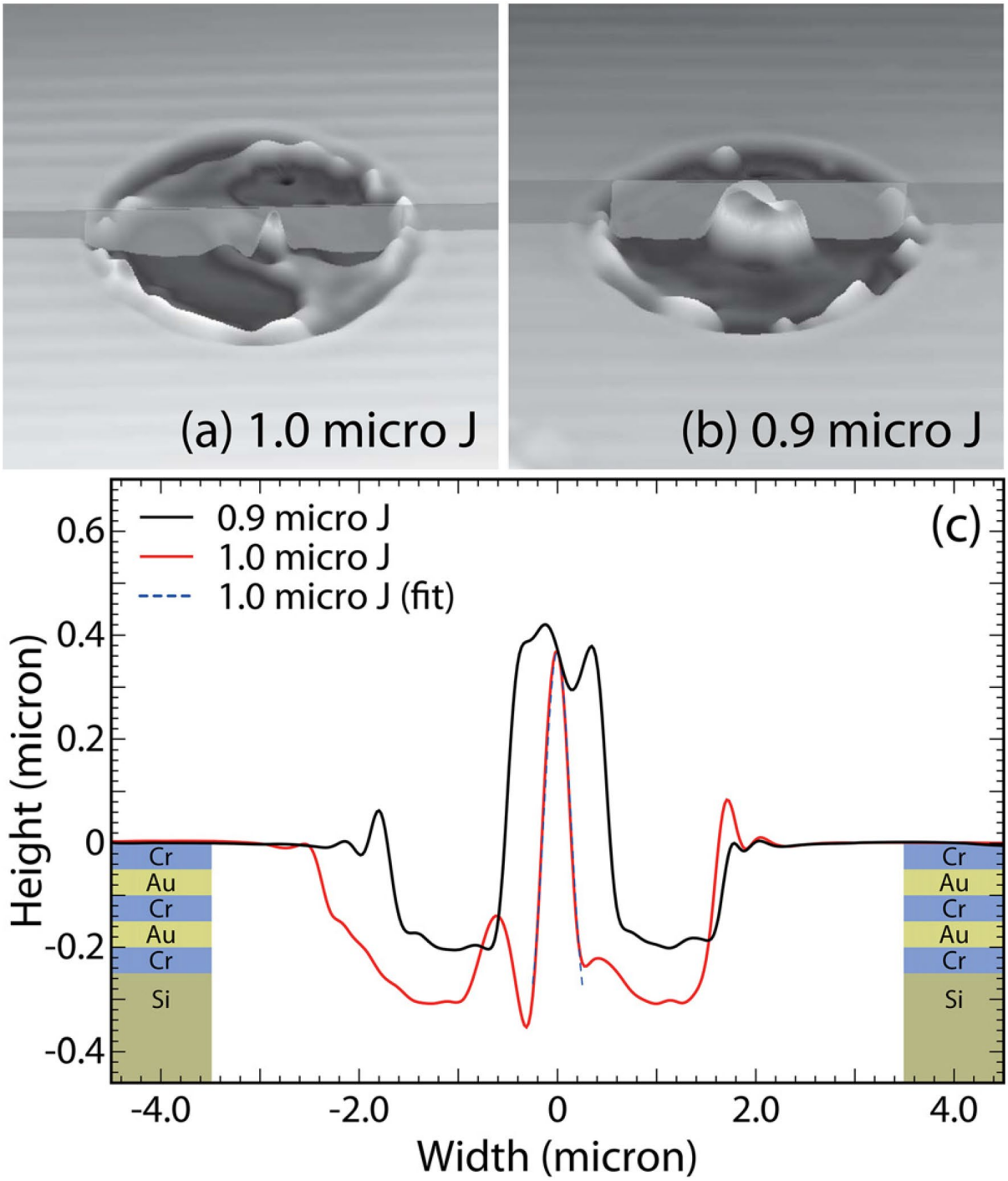

Figure 5.
Nanoneedles created on Cr/Au multi-layers by irradiation with an OAM x-ray pulse with different pulse energies (a) 1.0 μJ and (b) 0.9 μJ. (c) One-dimensional profiles of the needles along the planes in (a) and (b).
Reproduced with permission. [60] Copyright 2018, American Institute of Physics.

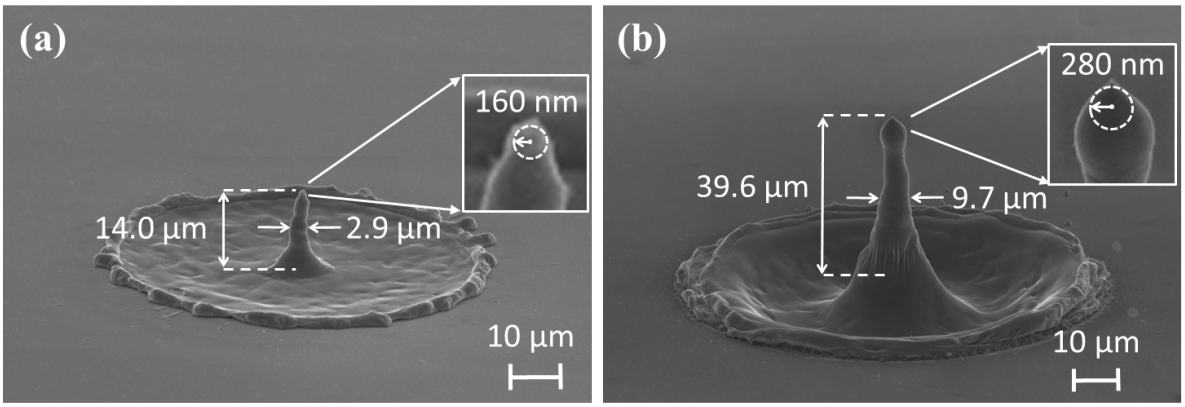

Figure 6.
Silicon nanoneedles created by irradiation with (a) a picosecond OAM pulse and (b) twelve overlaid OAM pulses.
Reproduced with permission.[22] Copyright 2016, Springer Nature.

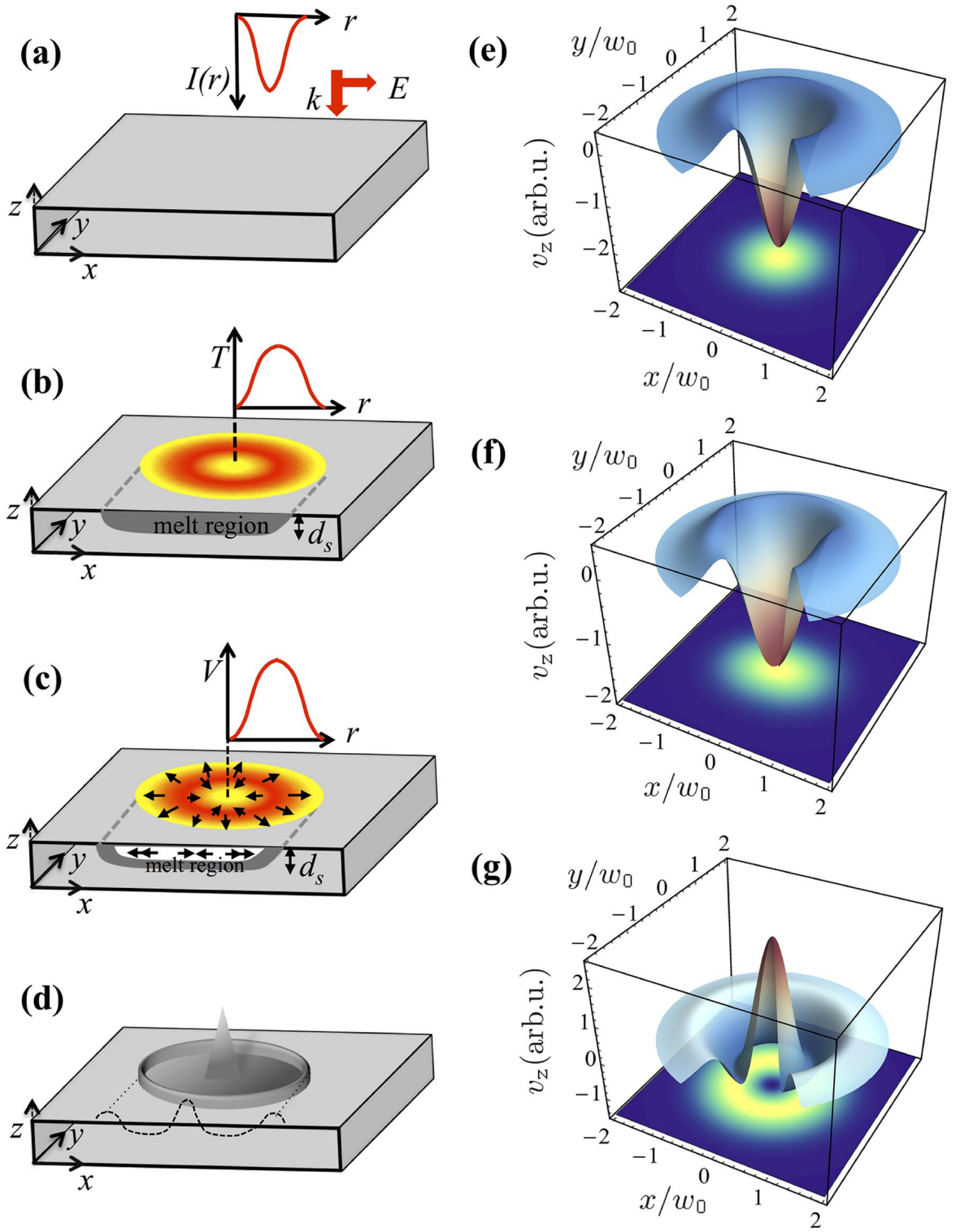

Figure 7.
Silicon nanoneedle formation with an OAM beam. (a-d) Schematic of rim and nano-cone formation process. (e-g) Mass transport for different temperature distributions. Reproduced with permission. [59] Copyright 2017, American Institute of Physics.

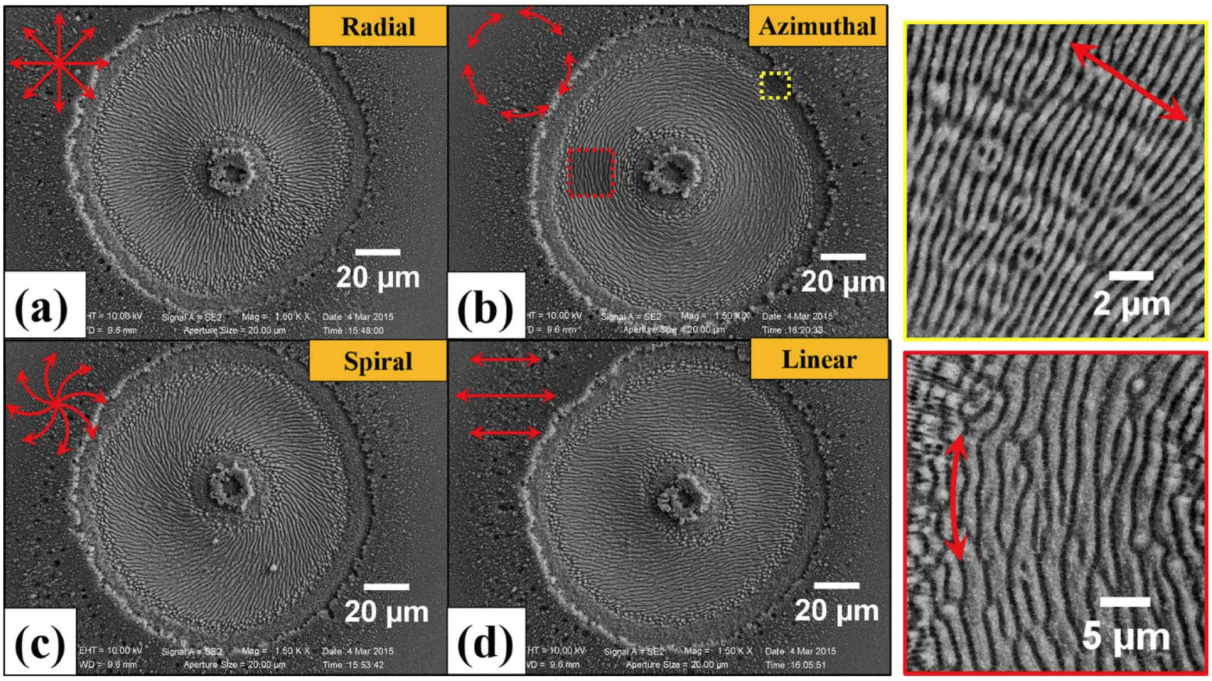

Figure 8.
Surface structures created on silicon by irradiation with OAM pulses with different polarizations: (a) radial, (b) azimuthal, (c) spiral and (d) linear. At the outer edges of the OAM beam, subwavelength ripples are oriented along the normal to the local laser polarization, while microgrooves are preferentially directed along the local laser polarization at the internal region of the OAM beam.
Reproduced with permission.[70] Copyright 2015, Springer Nature.

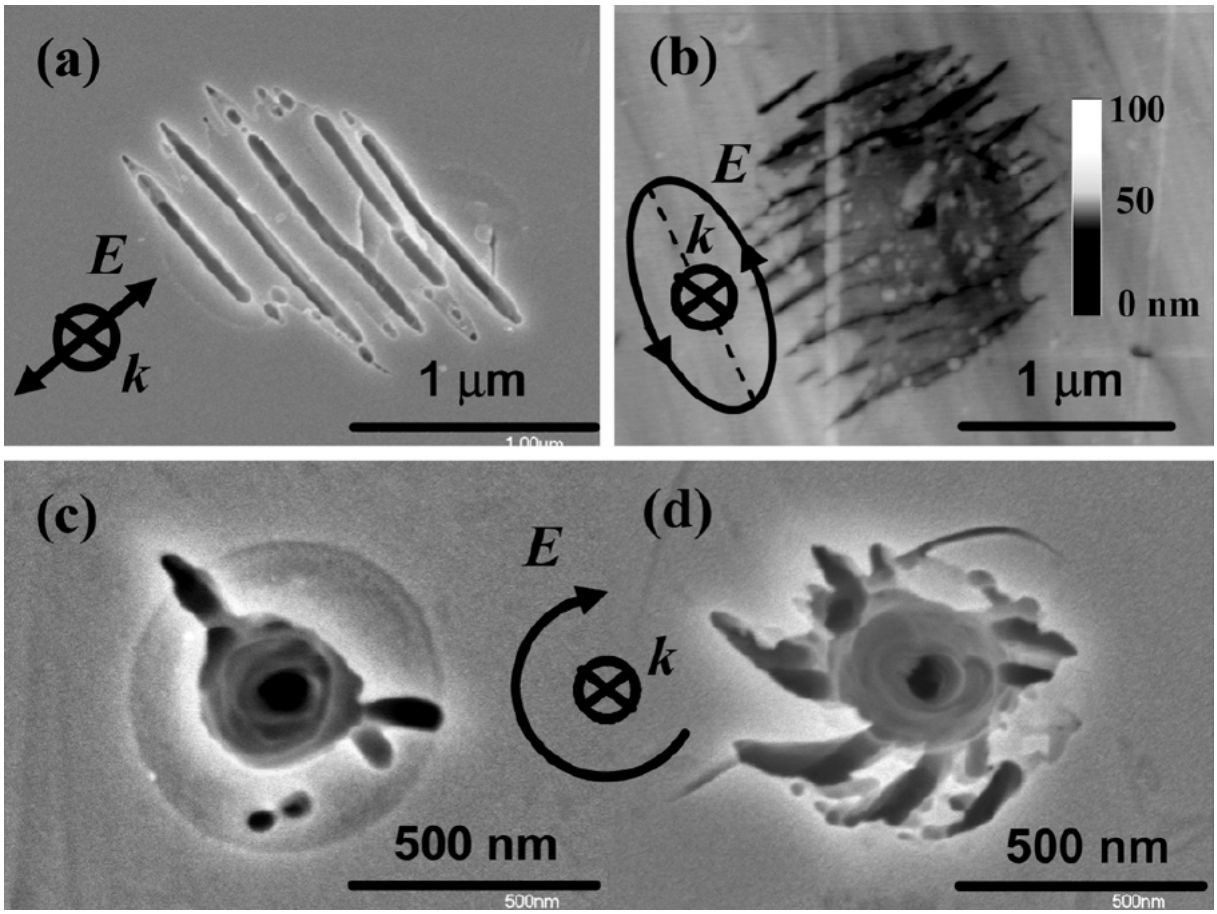

Figure 9.
Laser-induced structures formed inside fused silica glass. (a) linear polarization; (b) elliptical polarization; and (c) and (d) circular polarization.
Reproduced with permission.[71] Copyright 2008, The Optical Society.

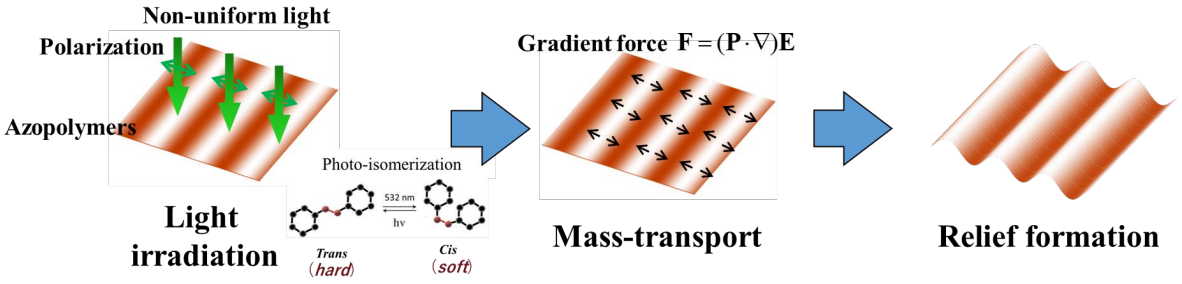

Figure 10
Schematic of surface relief formation in an azo-plymer film.

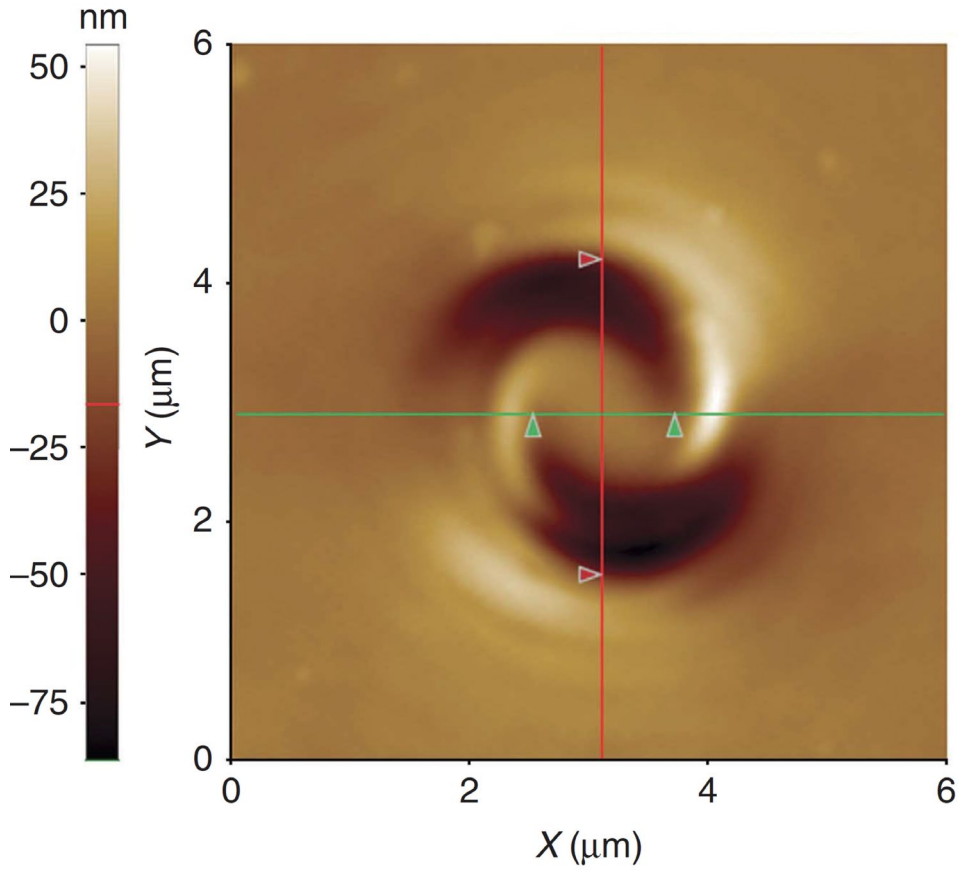

Figure 11.
"Spiral relief" created on an azo-polymer thin film by illumination with an OAM beam with ℓ=10.
Reproduced with permission.[79] Copyright 2012, Springer Nature.

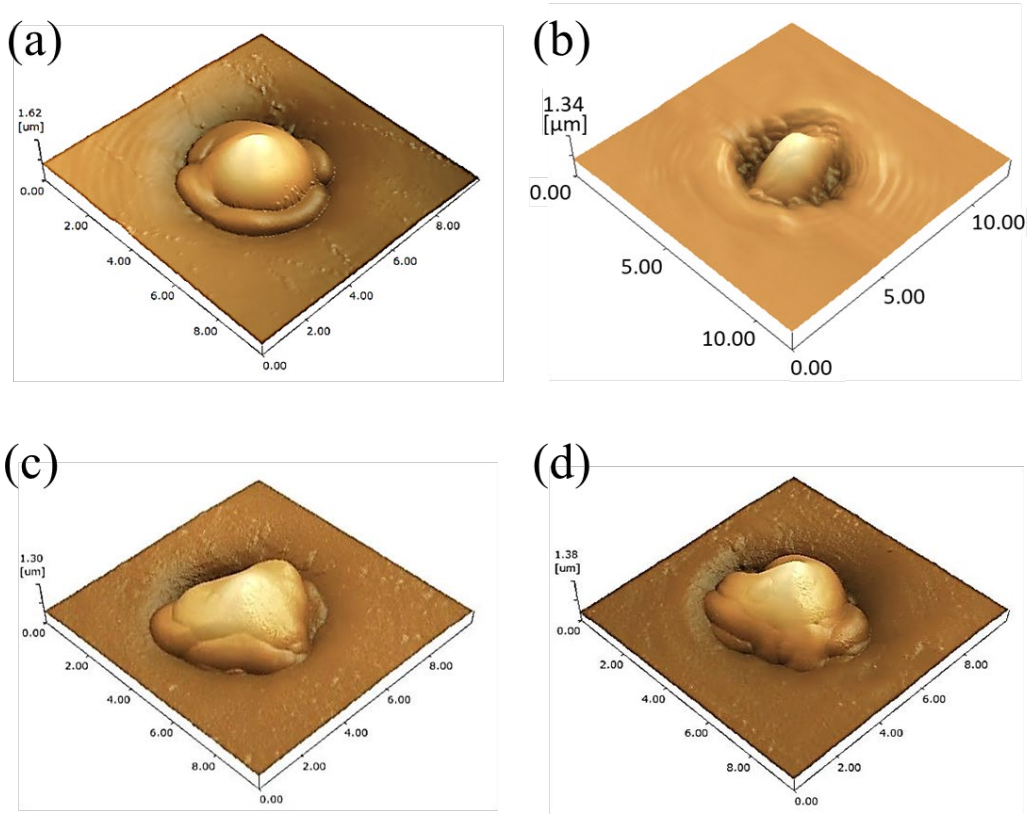

Figure 12.
Helical surface reliefs by illumination of azo-polymer with an OAM beam with (a) J=2 (ℓ=1, s=1), (b) J=2 (ℓ=2, s=0), (c) J=0 (ℓ=1, s=-1) and (d) J=0 (ℓ=-1, s=1).
Reproduced with permission.[23] Copyright 2014, Springer Nature.

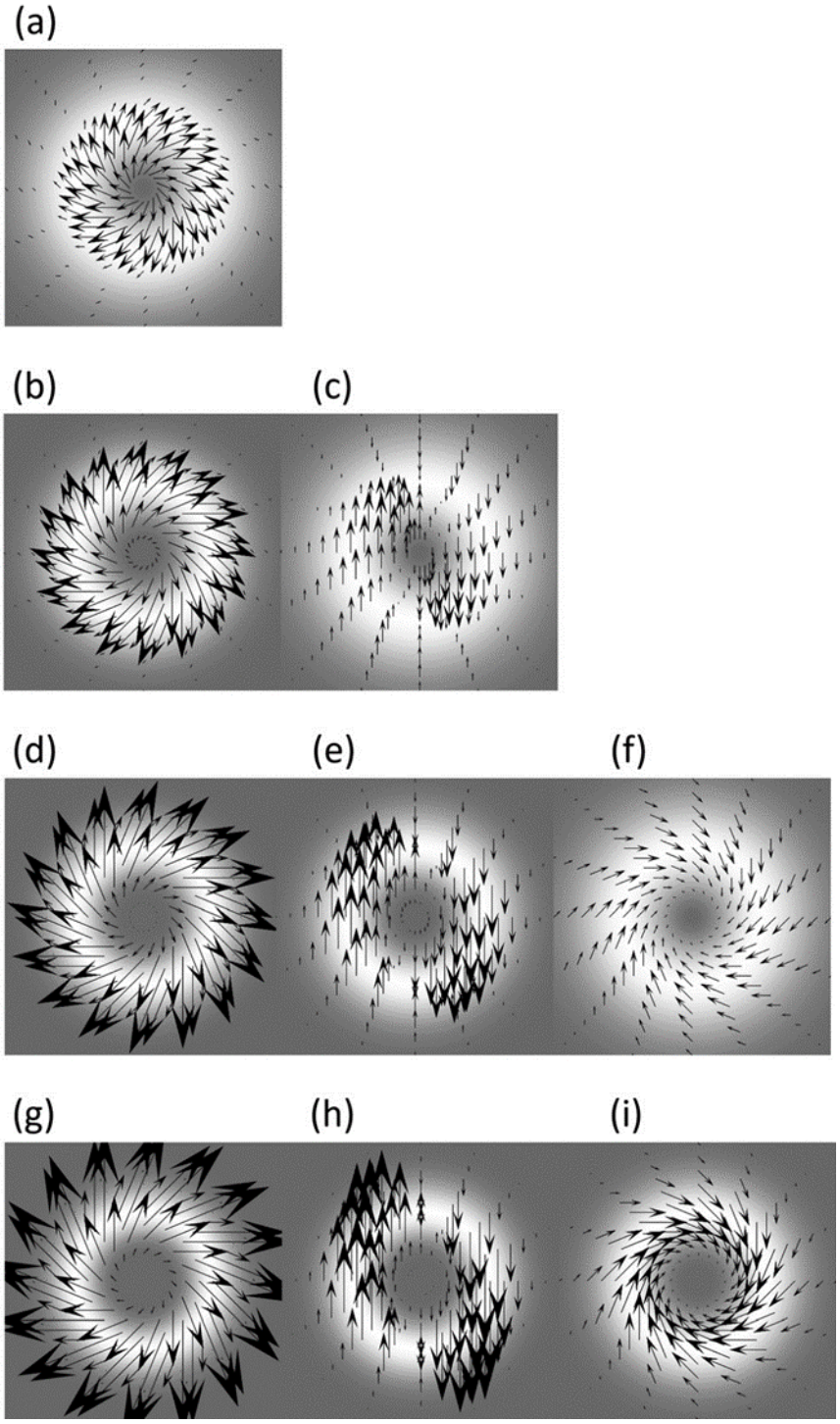

Figure 13.
Spatial distributions of radial and azimuthal forces produced by OAM beams with different TAM. (a) J=0 (ℓ=1, s=-1), (b) J=1 (ℓ=1, s=0), (c) J=1 (ℓ=1, s=0), (d) J=2 (ℓ=3, s=-1), (e) J=2 (ℓ=2, s=0), (f) J=2 (ℓ=3, s=-1), (g) J=3 (ℓ=4, s=-1), (h) J=3 (ℓ=3, s=0), and (i) J=3 (ℓ=2, s=1). Reproduced with permission.[80] Copyright 2016, American Institute of Physics.

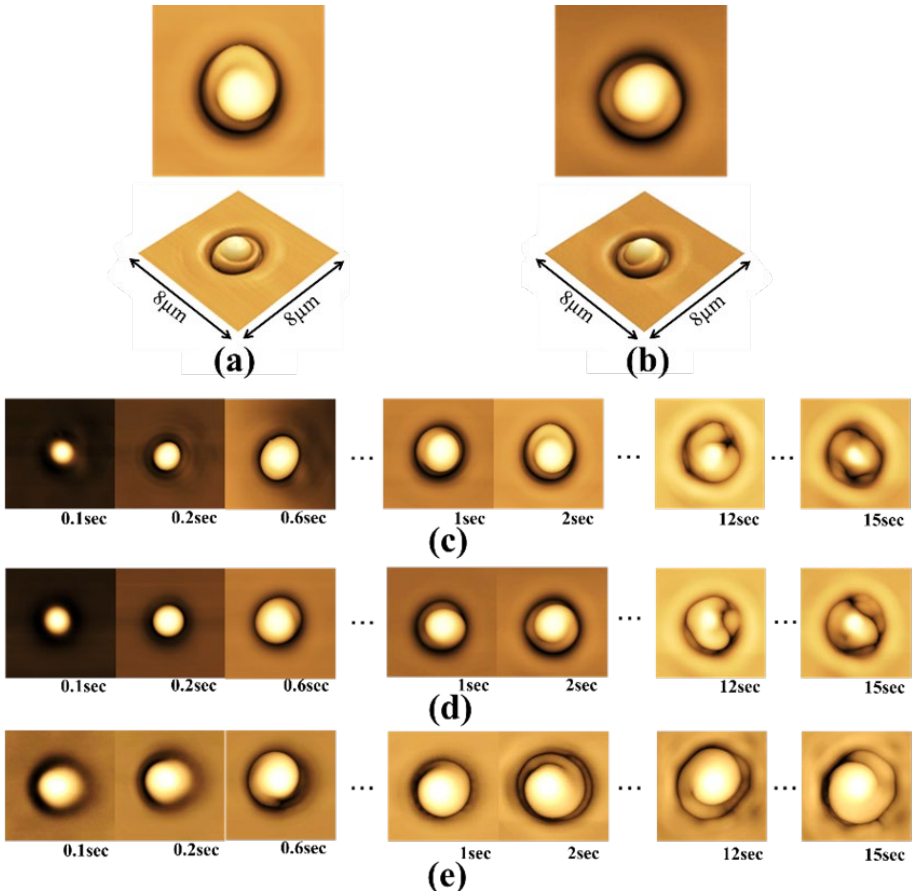

Figure 14.
Helical surface reliefs formed by illumination of azo-polymer with (a) right- and (b) left-handed circularly polarized beam and (c, d) their temporal evolution. (e) Right-handed surface relief formed by illumination with circularly polarized OAM beam with $J = 2$.
Reproduced with permission.[81] Copyright 2017, The Optical Society.

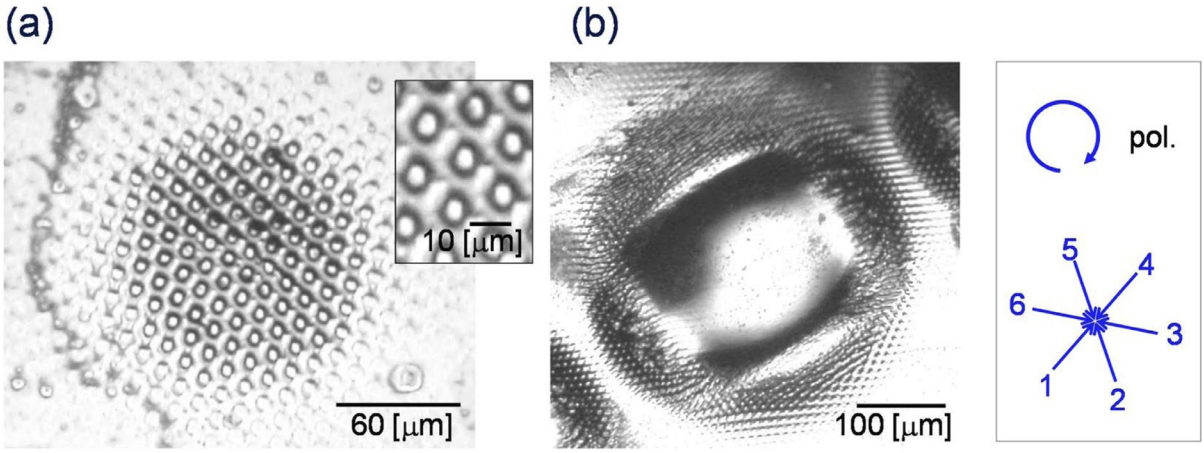

Figure 15
Multiple surface reliefs fabricated on an azo-polymer film by illumination with an interference pattern of six circularly polarized laser beams: (a) P = 35.8 mW and Δt = 6.0 seconds, (b) P = 71.6 mW and Δt = 10.0 seconds.
Reproduced with permission. [82] Copyright 2018, Springer Nature.

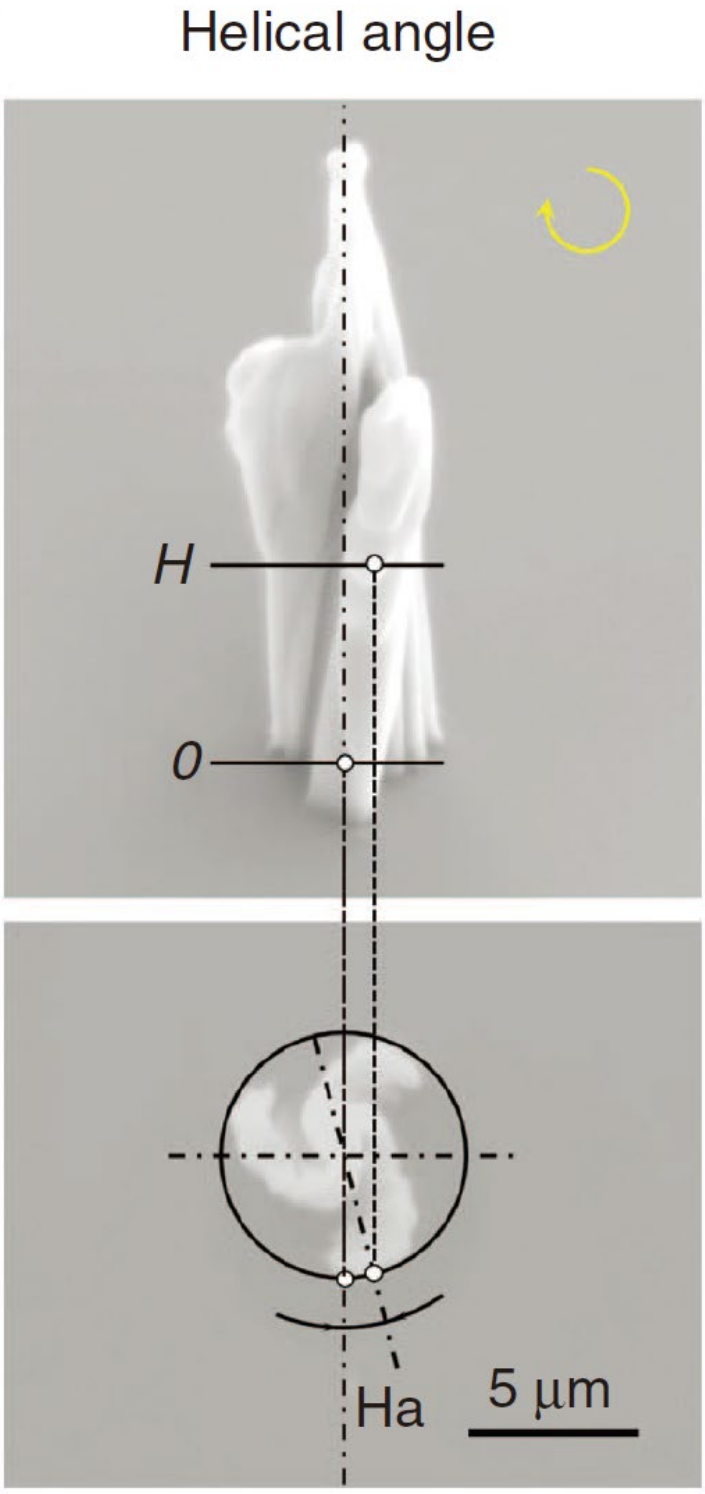

Figure 16
Aerial and top views of chiral microstructures created by irradiation of photopolymer resins by coaxial interference of a femtosecond vortex beam with a plane wave.
Reproduced with permission [89] Copyright 2017, The Optical Society.

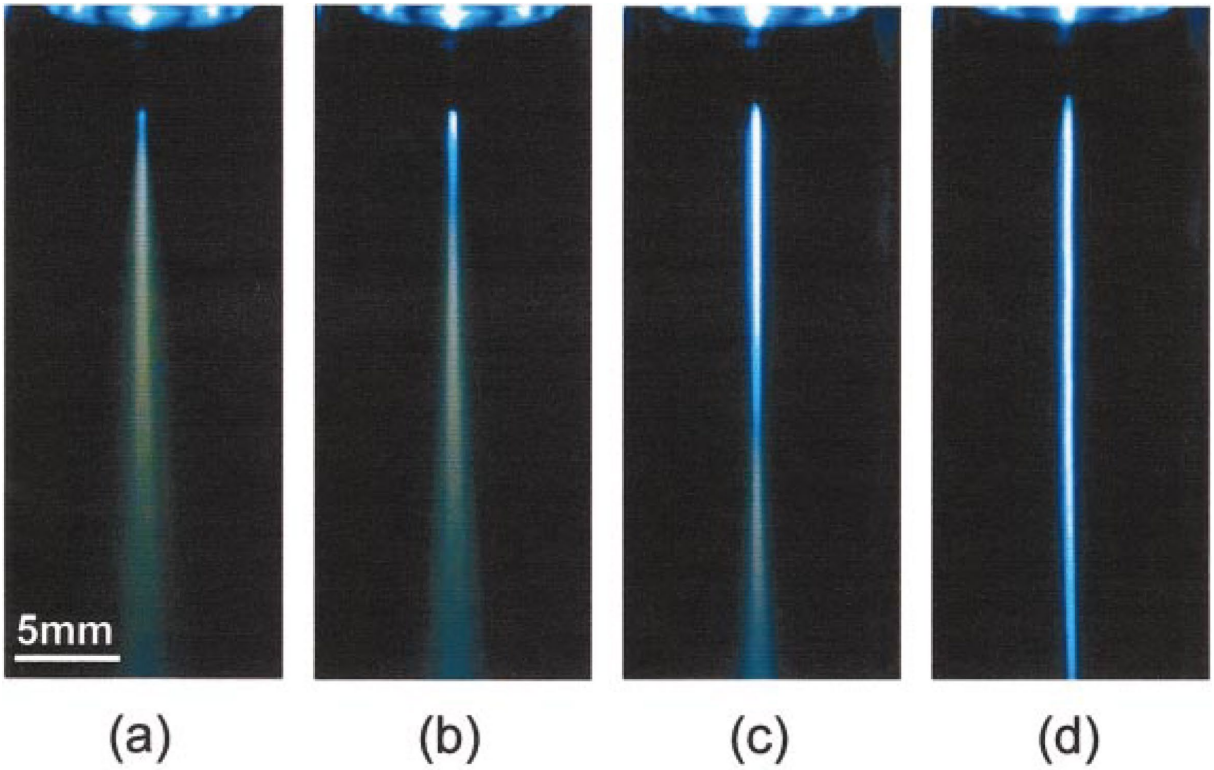

Figure 17
Temporal evolution of a laser-induced self-written optical waveguide formed in a photopolymer resin via optical fiber tip. Initial (a), intermediate (b, c) and final (d) stages. Reproduced with permission. [92] Copyright 2001, American Institute of Physics.

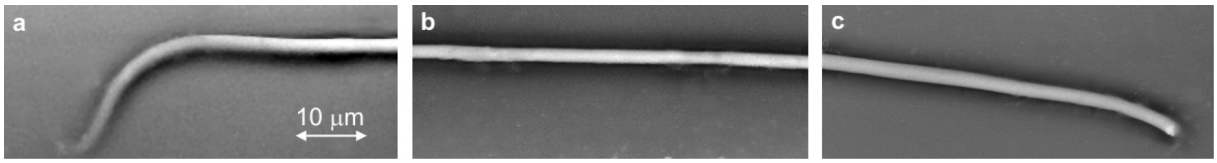

Figure 18
Microfiber structure polymerized by irradiation of a photopolymer resin with a Bessel beam. Left (a), middle (b) and right (c) part of the fiber.
Reproduced with permission.[93] Copyright 2006, The Optical Society.

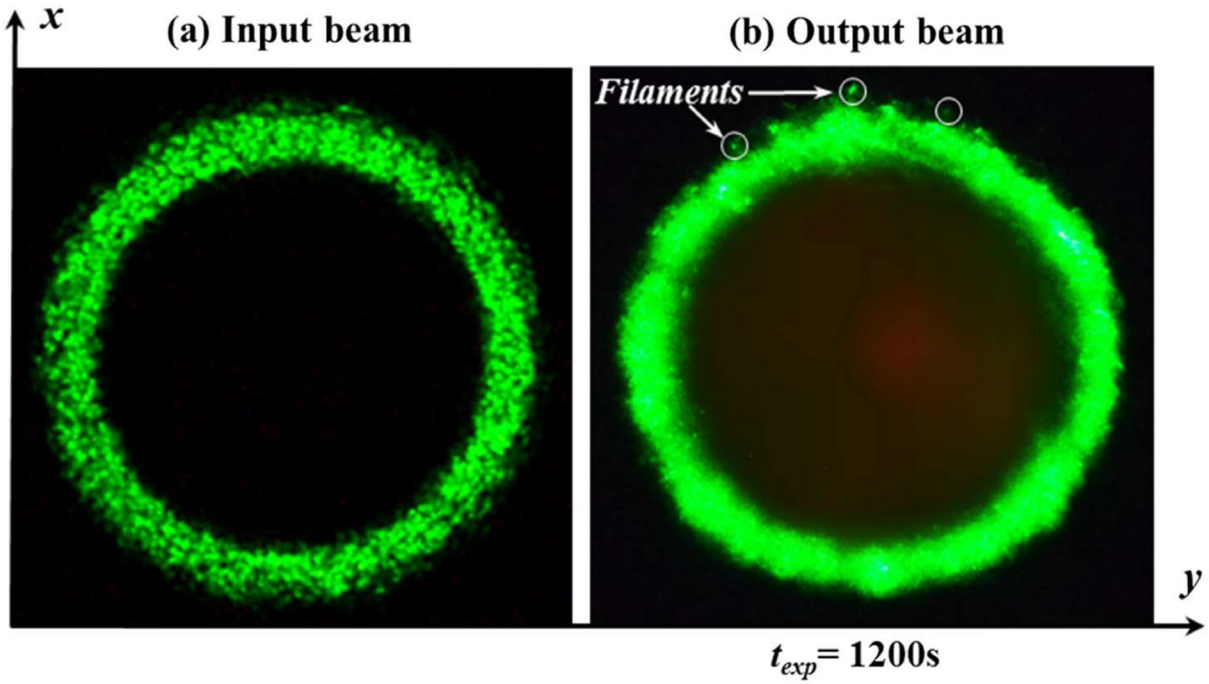

Figure 19
Photopolymerization of a resin by irradiation with an LG beam.
Reproduced with permission. [94] Copyright 2018, The Optical Society.

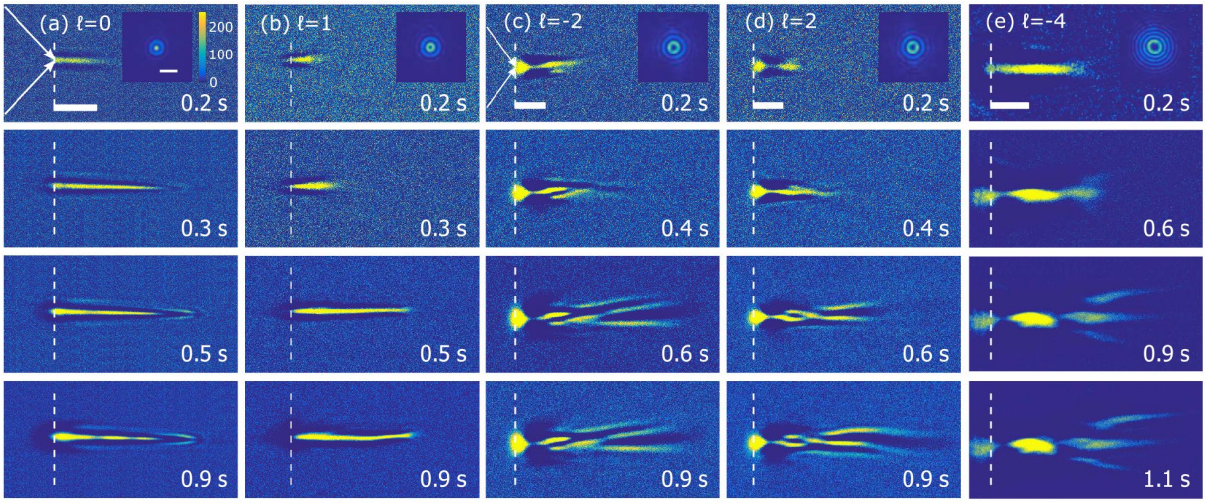

Figure 20.
Time-lapse images of the photopolymerization process. (a) ℓ= 0. (b) ℓ= 1, (c) ℓ= -2, (d) ℓ= 2, (e) ℓ= -4. White arrows indicate the beam focused at the glass/resin boundary (indicated as dashed lines). The scale bar shows 50 μm and applies to all figure panels.
Reproduced with permission.[24] Copyright 2018, American Chemical Society.

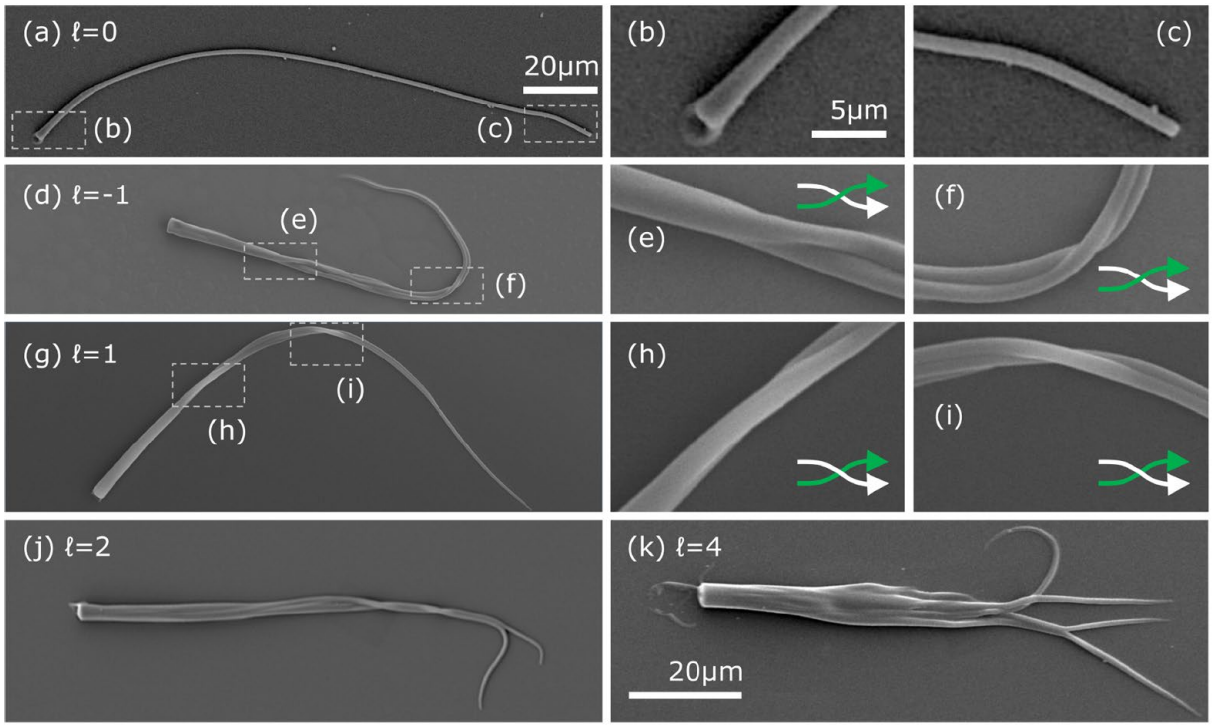

Figure 21.
Photopolymerized fiber created by laser irradiation with a Gaussian beam with ℓ=0 and LG beams with $|\ell|\geq 1$. (a) ℓ=0. (b, c) Expanded views of the selected areas in (a) showing the cylindrical structures. (d) ℓ=-1. (e, f) Expanded views of the selected areas in (d) showing the counterclockwise helix. (g) ℓ=1. (h, i) Expanded views of the selected areas in (g) showing the clockwise helix. (j) ℓ=2 exhibiting two fiber branches. (k) ℓ=4 exhibiting four branches. The 20 μm scale bar in panel (a) applies to (d), (g), and (j), while the 5 μm bar in panel (b) applies to (c), (e), (f), (h), and (i).
Reproduced with permission.[24] Copyright 2018, American Chemical Society.

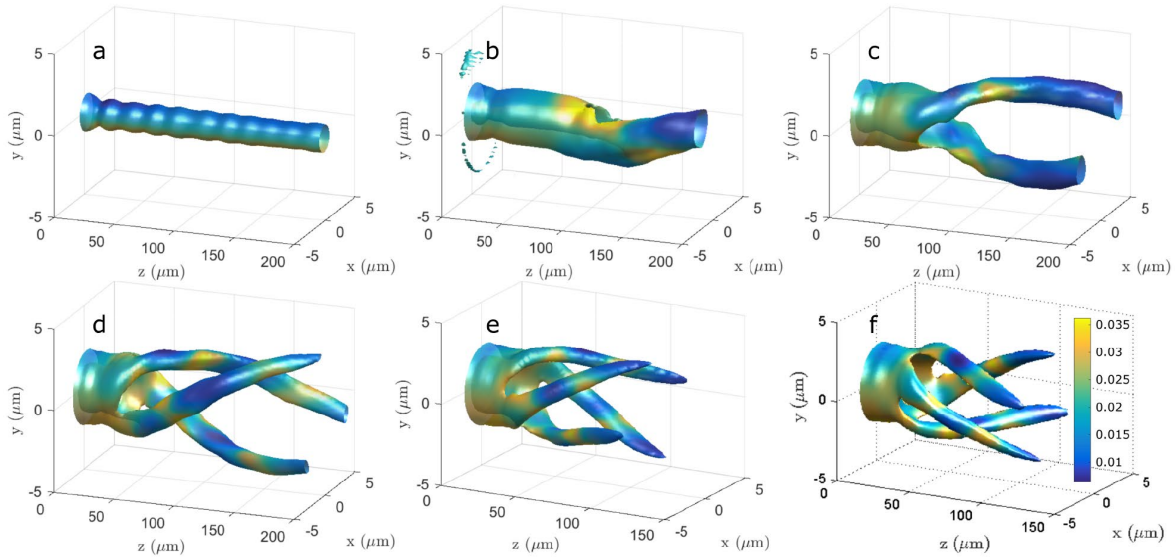

Figure 22.
Induced real index change $\Delta n'(r, t)$ evaluated at the exposure time t = 0.9 second showing the formation of helical microfibers during the photopolymerization process: (a) Gaussian beam (ℓ=0), (b) ℓ=1, (c) ℓ=2, (d) ℓ=3, (e) ℓ=4, and (f) ℓ=-4 showing the reversal of the chirality with respect to ℓ=4 in panel (e).
Reproduced with permission.[24] Copyright 2018, American Chemical Society.

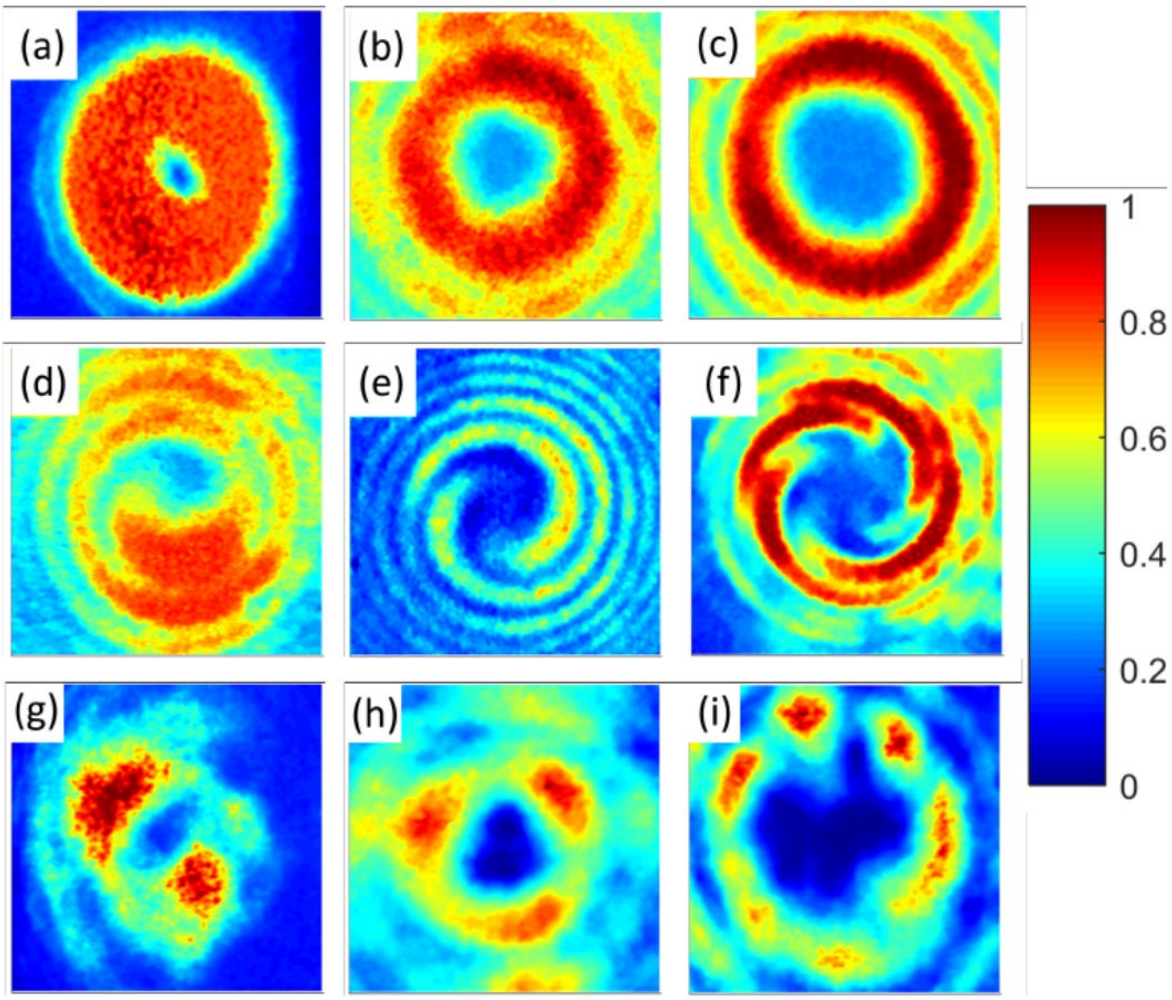

Figure 23.
Necklace beam formation in nonlinear colloidal suspensions with negative polarizability particles. (a–c) Intensity profiles and (d–f) interference patterns of the incident OAM beams of ℓ=1, 2, and 4. (g–i) Intensity distributions of the resulting necklace beams after the propagation in the colloidal medium corresponding to the incident beams in panels (a)–(c). Reproduced with permission.[96] Copyright 2018, American Chemical Society.